research papers

Cluster-packing geometry for Al-based F-type icosahedral alloys

Nobuhisa Fujita,[a]* Hikari Takano,[a] Akiji Yamamoto[b] and An-Pang Tsai[a,b]

[a]Institute of Multidisciplinary Research for Advanced Materials, Tohoku University, Sendai 980-8577, Japan, and [b]National Institute for Materials Science, Tsukuba 305-0044, Japan. Correspondence e-mail: nobuhisa@tagen.tohoku.ac.jp

This paper presents a new, highly stable, periodic approximant to the Al-based F-type icosahedral quasicrystals, i-Al–Pd–TM (TM = transition metals). The structure of this intermetallic Al–Pd–Cr–Fe compound is determined *ab initio* using single-crystal X-ray diffraction, where the space group is identified to be $Pa\overline{3}$ and the lattice constant 40.5 Å. The structure is well described as a dense packing of clusters of two kinds, which are called the pseudo-Mackay-type and the mini-Bergman-type clusters. Adjacent clusters can be markedly interpenetrated, while the structure requires no glue atoms to fill in the gaps between the clusters. It is shown that the clusters are centred at the vertices of a canonical cell tiling, which corresponds to a $2 \times 2 \times 2$ superstructure of Henley's cubic 3/2 packing, and that the parity of each vertex determines the kind of associated cluster. The proper quasi-lattice constant for describing the cluster packing is $1/\tau$ (τ = golden mean) times the conventional one used to describe Al-based P-type icosahedral alloys. The superstructure ordering of the present approximant turns out to be of a different kind from the P-type superstructure ordering previously reported in i-Al–Pd–Mn. The present results will greatly improve the understanding of atomic structures of F-type icosahedral quasicrystals and their approximants.

1. Introduction

The Al-based F-type icosahedral quasicrystals, such as i-$Al_{65}Cu_{20}Fe_{15}$ and i-$Al_{70}Pd_{20}TM_{10}$ (TM = transition metal, *e.g.* Mn, Re), pose a number of questions as to the detailed atomic arrangements. Researchers have tried to extract as much structural information as possible from materials of this kind through state-of-the-art techniques for structure analysis using X-ray, electron or neutron diffraction. These studies indicated that there existed a few different kinds of clusters as the basic building units that construct the quasicrystals.

A direct measurement of a quasicrystalline sample, however, entails a well known disadvantage in terms of structure determination. Conventional methods developed for analysing crystal structures are inherently inapplicable to quasicrystals owing to the absence of periodicity. However, these methods could still provide invaluable information regarding the constituent clusters as well as their local packing in quasicrystals through analysing their rational approximants. In particular, the latter approach has so far been taken successfully in elucidating local characteristics of P-type icosahedral quasicrystals, such as i-$Al_{73}Mn_{21}Si_6$ (Elser & Henley, 1985; Duneau & Oguey, 1989) and i-$Cd_{5.7}Yb$ (Takakura *et al.*, 2007).

Unfortunately, for the case of F-type icosahedral quasicrystals, a stable approximant phase has scarcely been reported. Hence, local characteristics of the structure have remained uncertain to a large extent. It appears as if Al-based F-type quasicrystals are so stable that no subordinate approximant phase could be obtained *via* a slight change of the composition. To date, only two possibly related cubic approximants have been previously reported in a rapidly quenched alloy with a nominal composition of $Al_{69}Pd_{20}Mn_8Si_3$ after annealing at above 1273 K (Ishimasa & Mori, 1992). By way of single-crystal X-ray diffraction, these approximants were determined to be cubic 1/1 and 2/1 approximants to the F-type icosahedral quasicrystal based on their lattice constants of 12.28 and 20.21 Å (Sugiyama *et al.*, 1998a,b). The structural information of the two refined structures has been utilized as the basis for building a six-dimensional structure model of the relevant F-type icosahedral quasicrystal (Yamamoto *et al.*, 2003). However, the reliability of the two structures has remained controversial because their constituent clusters were totally different despite their compositional similarity.

In i-$Al_{70}Pd_{20}TM_{10}$ and its close associates, Al, Pd and TM are likely to maintain their distinct roles in the structure. While no favourable approximant to the icosahedral quasicrystal has been reported for TM = Mn or Re, ample room remains for the choice of TM elements. In particular, a fine adjustment of the electron concentration (*e.g.* electron/atom ratio) could be achieved by mixing two transition metal elements for TM. In this report, the synthesis of a new stable

approximant is accomplished by blending Cr and Fe, the two immediate neighbours to Mn in the periodic table, for TM. An optimal ratio between Cr and Fe is searched for experimentally. The stability of the new phase is such that fine single crystals may grow through a simple slow-cooling method. Single-crystal X-ray diffraction is then performed to analyse the structure. The first part of this paper is devoted to a presentation of the synthesis and the crystal structure analysis.

The present structure analysis offers a source of information that is essential in understanding local atomic arrangements in the F-type icosahedral quasicrystals. It turns out that the structure is composed of two kinds of clusters, called the pseudo-Mackay-type and mini-Bergman-type clusters. The clusters are interconnected in such a way that significant interpenetrations are allowed, while no glue atom between them is required. Moreover, the centres of the clusters are given as the nodes (or vertices) of a three-dimensional tiling with four kinds of polyhedra called the canonical cells (Henley, 1991); this finding is of fundamental importance as it allows a systematic description of other related compounds as well as this particular one. The main body of the work comprises a full account of the crystal structure and related discussions.

The structural description can be generalized in a straightforward manner, leading to the proposal of a number of hypothetical structures which could form as real approximants. Although a full description of the F-type icosahedral quasicrystals awaits future endeavours, our understanding of the local atomic arrangements in the F-type icosahedral quasicrystals and their approximants can now be revised significantly based on firm experimental evidence. This paves the way for further attempts to synthesize variants of stable approximants as well as to gain insights into the superlattice ordering phenomenon which was reported previously in the F-type icosahedral quasicrystal i-$Al_{70}Pd_{20}TM_{10}$ (Ishimasa, 1995).
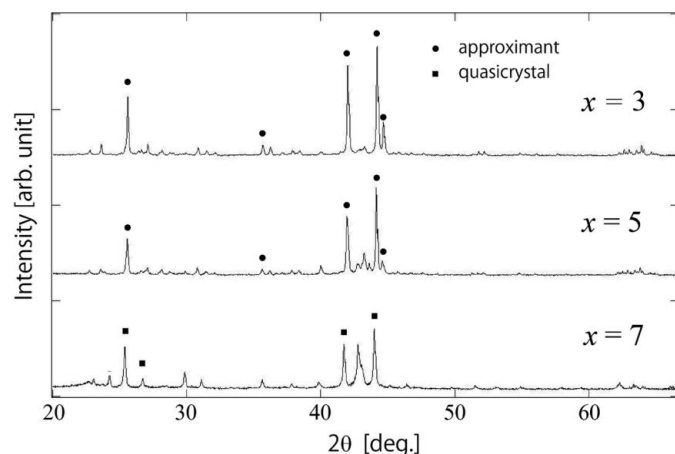
Figure 1
Powder X-ray diffraction diagrams for $Al_{70}Pd_{20}Cr_xFe_{10-x}$ (x = 3, 5 or 7). For x = 3 and 5, the peaks marked with filled circles are associated with an approximant, while for x = 7 those marked with filled squares are associated with a quasicrystal. Note that unassigned peaks associated with impurity phases become prominent as x is increased.

This paper is organized as follows. §2 illustrates how a simple compositional search culminates in the discovery of a new approximant phase. The initial samples were polycrystalline, yet powder X-ray diffraction as well as electron diffraction proves the presence of a cubic approximant with a large unit cell. An electron probe micro-analyser (EPMA) is used to evaluate the fine chemical composition of the approximant. Then an optimized synthesis is performed, resulting in the growth of single crystals exceeding 100 μm in diameter. Single-crystal X-ray diffraction and the structure analysis are reported in §3. The crystal structure is described in detail in §4 in a constructive manner. After introducing the geometrical templates of the two kinds of cluster, the packing geometry of the clusters is described in detail. It is shown that the global arrangement of the clusters is determined based on a canonical cell tiling with F-type ordering. In an early part of §5, we discuss the relationship between a superlattice ordering of the present approximant and that in the quasicrystal. The likelihood of anti-phase boundaries as a possible source of disorder in the present material is also discussed. The remainder of this section examines the possibility of introducing a tiling model for the atomic arrangement. §6 is devoted to concluding remarks.
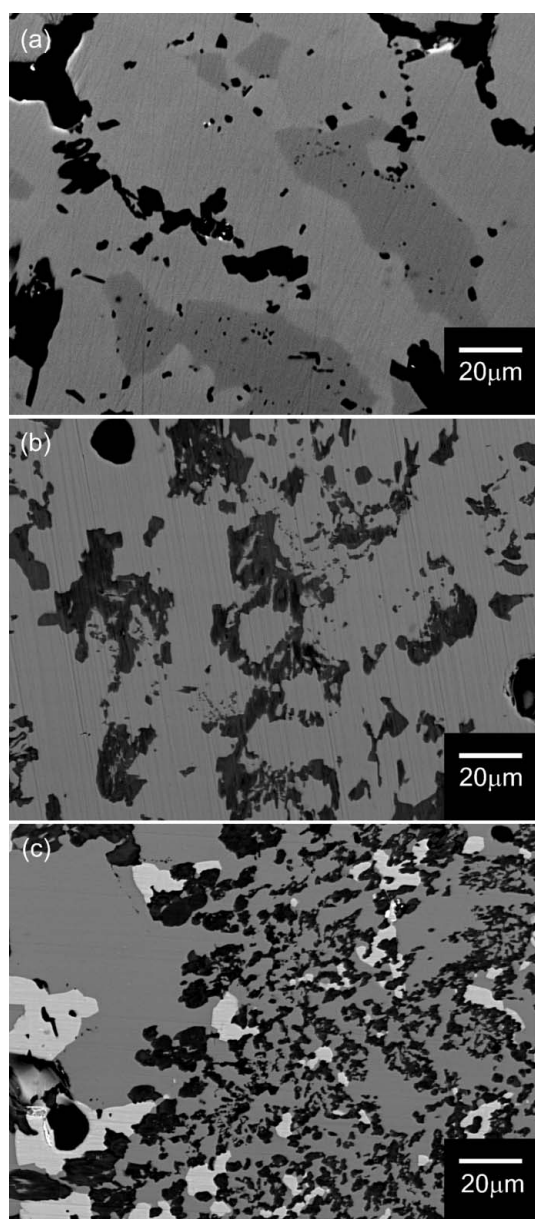
2. Synthesis and characterization

Our synthesis of the new approximant was performed in two steps. Firstly, a search for a possible approximant phase was made by varying the ratio between Cr and Fe. A few characterization techniques were used to locate the composition of the approximant phase as well as to extract the basic crystallographic information. Secondly, starting from the right composition a new synthesis was performed with slow cooling. High-quality single crystals of the approximant were successfully obtained in this way. These steps are described in the following.

The starting materials were Al (Kojundo Chemical Laboratory; purity 99.9%), Pd (Tanaka Kikinzoku; purity 99.95%), Cr (Furuuchi Chemical; purity 99.9%) and Fe (Nilaco; purity 99.5%). An alloy ingot with a nominal composition of $Al_{70}Pd_{20}Cr_xFe_{10-x}$ (x = 3, 5 or 7) was prepared by the arc-melting method under an argon atmosphere. After sufficient homogenization was achieved, the as-solidified ingot was fragmented, put into a Tammann crucible made of Al_2O_3 and sealed altogether into a quartz tube with pure argon gas of about 0.08 MPa. In an electric furnace, the sample was annealed at 1123 K for 48 h and cooled swiftly (~1 h) down to room temperature.

In Fig. 1, powder X-ray diffraction patterns taken from the samples x = 3, 5 and 7 are shown, where the characteristic X-ray of Cu $K\alpha$ (λ = 1.543 Å) is used with Bragg–Brentano diffraction geometry (Mac Science, diffractometer M03XHF[22]). Slightly above the strongest Bragg peak at $2\theta \sim 44°$, a clear sub-peak is observed for the two samples x = 3 and 5. The latter peak feature is usually associated with the cubic 2/1 approximant to an icosahedral quasicrystal with the Miller indices being hkl = 10 0 0. The corresponding lattice constant

is calculated to be about 20.3 Å. The sample $x = 3$ appears to contain the largest amount of the approximant phase, while the suppression of the sub-peak as well as the growth of an extra feature at $2\theta \sim 43°$ clearly indicate the prevalence of impurity phase(s) as x is increased. Hence, it is expected that $Al_{70}Pd_{20}Cr_3Fe_7$ is the closest composition to that of the approximant phase.

Back-scattered electron images taken from the three samples using a scanning electron microscope are shown in Fig. 2. The scanning electron microscope apparatus used is a JXA-8621MX (Jeol), in which an EPMA is implemented for chemical composition analysis. A few domains of different grey levels are observed in each sample (voids are shown as black regions), indicating the existence of a few alloy phases with different compositions. It is observed that a light-grey region in Fig. 2(a) represents the majority phase for $x = 3$ with

Figure 2
SEM (scanning electron microscopy) back-scattered electron images for (a) $x = 3$, (b) $x = 5$ and (c) $x = 7$. The estimated compositions are: (a) $Al_{69.1}Pd_{22.0}Cr_{2.1}Fe_{6.8}$ (light grey) and $Al_{68.4}Pd_{20.9}Cr_{1.1}Fe_{9.5}$ (dark grey), (b) $Al_{69.7}Pd_{22.5}Cr_{2.3}Fe_{5.4}$ (light grey) and $Al_{72.5}Pd_{11.8}Cr_{11.6}Fe_{4.0}$ (dark grey) and (c) $Al_{69.5}Pd_{23.5}Cr_{3.6}Fe_{3.4}$ (light grey) and Al_3Pd_2 (white).
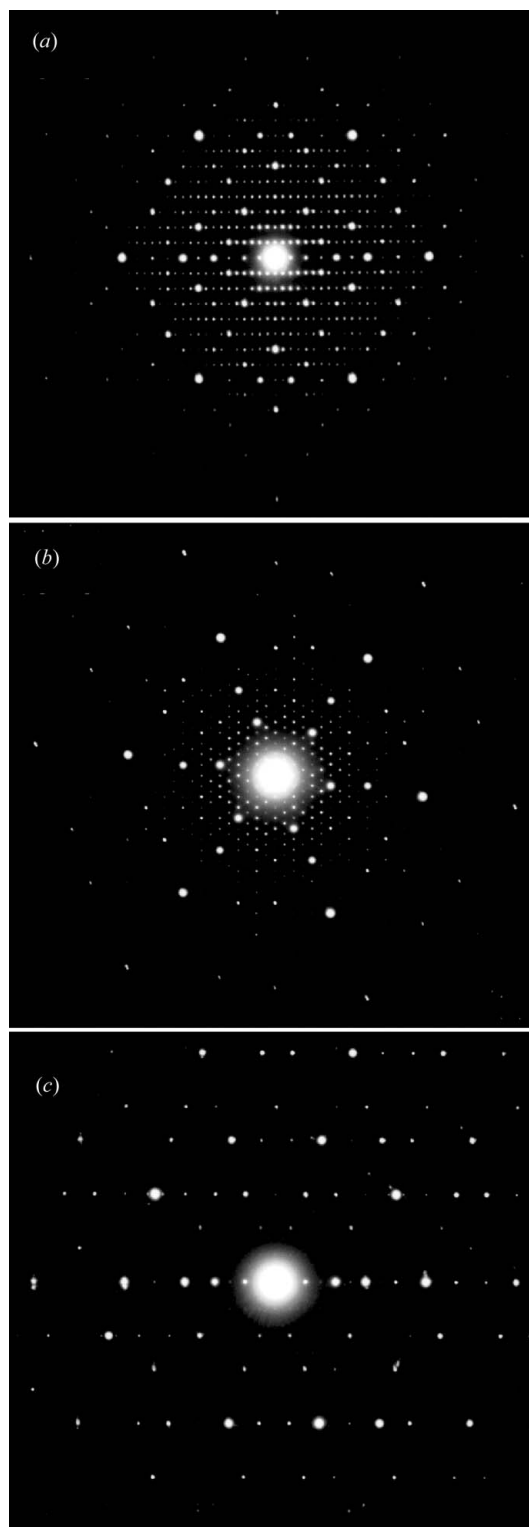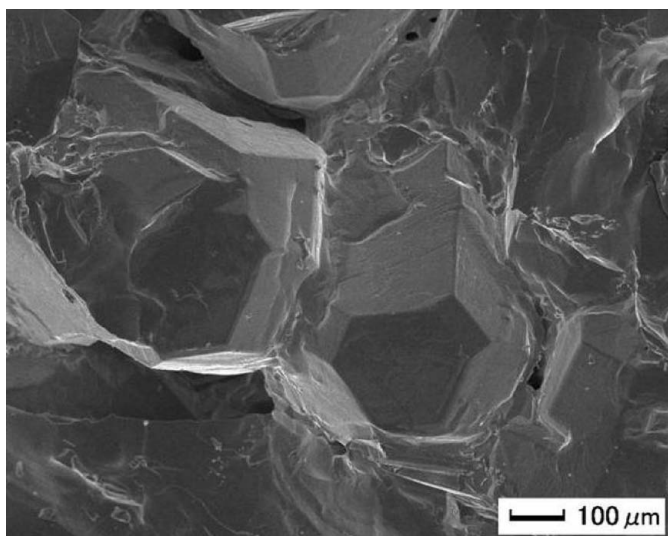

Figure 3
TEM (transmission electron microscopy) diffraction patterns taken from the $Al_{70}Pd_{20}Cr_3Fe_7$ sample along (a) the twofold axis ($\parallel \langle 100 \rangle$), (b) the threefold axis ($\parallel \langle 111 \rangle$) and (c) one of the pseudo-fivefold axes.

the estimated composition being $Al_{69.1}Pd_{22.0}Cr_{2.1}Fe_{6.8}$. It is reasonable to assume that this region corresponds to the approximant, which constitutes the main body of the sample. For $x = 5$, a light-grey region in Fig. 2(b) has an estimated composition of $Al_{69.7}Pd_{22.5}Cr_{2.3}Fe_{5.4}$ and one can still associate it with the approximant, as the compositional difference is insubstantial. However, all the phases observed for $x = 7$ deviated significantly from the approximant in terms of chemical composition, implying no relevant approximant phase exists in the sample.

Firmer evidence of the approximant phase was provided by selected-area electron diffraction. Here a JEM-2000EXII (Jeol) transmission electron microscope operating at 200 kV was used. Electron diffraction patterns taken from the $Al_{70}Pd_{20}Cr_3Fe_7$ sample (Fig. 3) clearly indicate the existence of twofold, threefold and pseudo-fivefold axes, where strong Bragg reflections are arranged in a similar way to the case of the quasicrystal (Tsai *et al.*, 1990). In Figs. 3(a) and 3(b), periodic arrays of spots can be indexed as a cubic crystal with a lattice constant of about 40 Å. Note that, however, this is twice as large as the one estimated from the above powder X-ray diffraction pattern by assuming a conventional 2/1 approximant. Moreover, extinctions are observed at $0kl$ with $k = $ odd and at $00l$ with $l = $ odd, indicating that the crystal has a nonsymmorphic space group. Therefore, the pre-existing model of 2/1 approximant with the space group $Pm\overline{3}$ (Sugiyama *et al.*, 1998b; Dmitrienko & Chizhikov, 2007) clearly fails to describe the present material. This motivated us to investigate the crystal geometry based on an *ab initio* structure determination using single-crystal X-ray diffraction.

In order to obtain a single crystal to be used for the structure analysis, a new sample was prepared in the following way. A refined composition given by the arithmetic mean, $Al_{69.4}Pd_{22.3}Cr_{2.2}Fe_{6.1}$, of the two compositions evaluated from the samples $x = 3$ and 5 was used for the starting composition. The preparation steps were the same as those described above

Figure 4
SEM micrograph taken from the single-crystalline sample obtained with a nominal composition of $Al_{69.4}Pd_{22.3}Cr_{2.2}Fe_{6.1}$.

except that at the annealing step within the furnace the sample was fully melted at 1433 K for 1 h and then cooled down slowly to room temperature with a cooling rate of 10 K h^{-1}. Fig. 4 shows a scanning electron microscopy (SEM) micrograph taken from the new sample using the JCM-5100 (Jeol), where faceted crystalline grains roughly in the shape of a truncated octahedron are wrapped partially with debris (impurities). It confirms that single crystals a few hundred μm in diameter were successfully grown, which also implies that the approximant formed congruently from the melt.

3. *Ab initio* structure determination

3.1. Single-crystal X-ray diffraction

A single crystal was taken from the new sample with estimated dimensions of $0.272 \times 0.178 \times 0.320$ mm. The diffraction experiments were performed using a Bruker SMART APEX diffractometer, mounting CCD area detector, with Mo $K\alpha$ radiation and graphite monochromator (wavelength 0.71073 Å). Indexing and empirical absorption correction were performed using the Bruker software package (*SMART*, *SAINT* and *SADABS*; Bruker, 2001). In collecting the reflection intensities, the crystal was identified as a primitive cubic crystal with a lattice constant of 40.54 Å.

Inspecting the original reflection data, it was found that a set of symmetrically equivalent reflections often included one or a few members showing exceptional deviation in the intensity. This is due to the dynamical effect (or multiple scattering) by which an extra intensity is added to the 'kinematical' Bragg intensity. Although the extra intensities are weak in contrast to those of the strongest Bragg reflections, they could still be harmful for weak reflections; note that the structural information carried by weak reflections plays a crucial role in determining the long-range characteristics of a complex structure such as a quasicrystal and an approximant with a large unit cell.

In principle, a reflection intensity affected by multiple scattering could be effectively screened out from the data based on the intensity distribution among the set of equivalent hkl entries. In a common structure-refinement software (*e.g.* *JANA2006*; Petricek *et al.*, 2006), the procedure can be performed when equivalent reflections are averaged. However, if the number of equivalent hkl entries is small, the statistics are simply not enough to discern the ill-entry. Hence, we took a precaution to remove those hkl entries which have less than six symmetrically equivalent associates from the original data set in order to avoid the possible source of error. The pre-processed data set was used for the structure analysis as described in the following subsection.

3.2. Structure analysis

Our structure analysis relied entirely on the *JANA2006* software package (Petricek *et al.*, 2006). The Laue group and the space group were determined unambiguously to be $m\overline{3}$ (T_h) and $Pa\overline{3}$, which turned out to be the only nonsymmorphic space group with minor contradictions with the
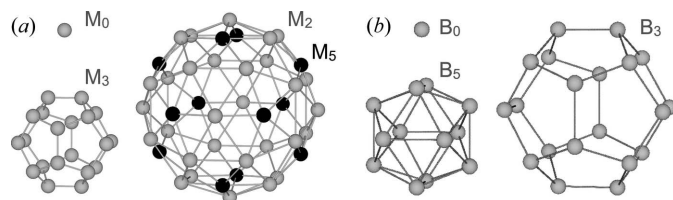
Table 1
Crystallographic data.

Formula	$Al_{72.515}Pd_{22.498}Cr_{4.928}Fe_{7.853}$
Molar mass	5045.2 g mol^{-1}
Temperature of data collection	Room temperature
Space group	$Pa\overline{3}$ (No. 205)
Lattice constant, a_{lat}	40.5405 Å
Cell volume, Ω	66629.6 Å^3
Z	40
Calculated density	5.028 g cm^{-3}
Absorption coefficient	9.294 mm^{-1}
Range of 2θ	1.74–53.2°
Independent reflections	21526
Observed reflections [$I > 3\sigma(I)$]	8454
R_{int} (obs/all)	7.91/13.37
No. of parameters	783
$R(F)$	11.96
$R_w(F)$	12.13
S	4.59
$\Delta\rho_{max}$, $\Delta\rho_{min}$	8.01, -5.38 e Å^{-3}
$\Delta/e.s.d.$	0.0002

data. Out of the whole 95 213 observed reflections satisfying $I > 3\sigma(I)$, 302 symmetrically extinct reflections were included. The symmetry averaging was performed while at the same time those data entries showing significant deviation from the averages of their equivalent reflections [$|I - I_{av}| > 10\sigma(I_{av})$] were eliminated from the data. The averaged data containing 8454 independent reflections satisfying $I > 3\sigma(I)$ were obtained with $R_{int} = 7.91\%$.

The initial structure model was generated with the *SUPERFLIP* program (Palatinus & Chapuis, 2007), which is an implementation of the charge-flipping algorithm in *JANA2006*. Then Fourier synthesis and least-squares fitting were iterated. After several iterations, the automated peak search became unsuccessful in locating new atoms. Then we carefully inspected the tentative structure, finding incomplete icosahedral clusters orderly packed in the unit cell. We identified two kinds of clusters, which have been known as the pseudo-Mackay-type clusters and the mini-Bergman-type clusters. It was observed that adjacent clusters were connected along either a twofold or a threefold symmetry axis of the reference icosahedron; a twofold linkage connects clusters of the same kind and a threefold linkage connects ones of different kinds. After the central atoms of all the clusters were identified, the missing atoms within each cluster were located by inspecting the charge-density plot. Finally the refinement

converged with reliability indices of $R(F) = 11.96\%$ and $R_w(F) = 12.13\%$. Basic crystallographic data are summarized in Table 1. A detailed presentation of the refinement is provided in Appendix B. The reader may consult the online supplementary material[1] for a high-resolution powder X-ray diffraction pattern measured with synchrotron radiation along with a simulated pattern for the refined structure; a comparison between the two lends further credibility to the refinement.

4. Crystal structure

The refined structure contains 4728 atomic sites per unit cell, wherein 204 sites are symmetrically independent. Importantly, the structure can be pictured as one formed through a dense packing of clusters, which are allowed to overlap with each other across their peripheries. There is no need for glue atoms to fill in the gaps between the clusters, meaning each of the atomic sites belongs to at least one cluster. Two kinds of clusters called the pseudo-Mackay-type and the mini-Bergman-type clusters are identified; these are henceforth referred to as M- and B-clusters, respectively.

4.1. Cluster templates

The geometrical templates for the M- and B-clusters are shown in Fig. 5; both have an atomic site at the centre and two shells having the full icosahedral symmetry, $\overline{5}32/m$ (I_h). The central sites are symbolized as M_0 and B_0 for the M-cluster and B-cluster, respectively. The inner shell of the M-cluster consists of 20 sites forming the vertices of a regular dodecahedron. This shell is symbolized as M_3 because the relevant sites are on the threefold rotation axes of the icosahedral point group; the same principle also applies when symbolizing the remaining shells. The outer shell of the M-cluster is a composite of two subshells, 12 sites forming a regular icosahedron (M_5) and 30 sites forming a regular icosidodecahedron (M_2). On the other hand, the inner shell of the B-cluster consists of 12 sites forming a regular icosahedron (B_5), while the outer shell has 20 sites forming a regular dodecahedron (B_3).

Let us now define the six icosahedral basis vectors $\mathbf{a}_j$ ($j = 1, 2, \ldots, 6$) as

$$(\mathbf{a}_1 \ \mathbf{a}_2 \ \mathbf{a}_3 \ \mathbf{a}_4 \ \mathbf{a}_5 \ \mathbf{a}_6)$$
$$:= \ell \begin{pmatrix} \tau & 0 & 1 & 1 & -\tau & 0 \\ 1 & \tau & 0 & 0 & 1 & -\tau \\ 0 & 1 & \tau & -\tau & 0 & 1 \end{pmatrix}, \quad (1)$$

where $\tau = (1 + 5^{1/2})/2$ is the golden mean and ℓ represents an appropriate scale. The norm of the basis vectors is hereafter denoted $a(:= |\mathbf{a}_j|)$. Note that the numbering, $j = 1, 2, \ldots, 6$, of the six basis vectors is taken such that they are arranged concentrically around a threefold rotation axis.[2] Taking the

Figure 5
The idealized templates for the two kinds of cluster. (*a*) The M-cluster consists of a central site (M_0), a dodecahedral shell (M_3) and a composite shell with an icosahedral subshell (M_5) and an icosidodecahedral subshell (M_2). (*b*) The B-cluster consists of a central site (B_0), an icosahedral shell (B_5) and a dodecahedral shell (B_3).

Table 2
The indices given for each shell represent the vector from the centre to a representative site of the shell.

Representative vectors for b- and c-linkages as well as the lattice translation vectors are also given for reference. The norm of each vector (namely, the radius of the shell) is given in the right column. Note that $b = 2(\tau^3/5^{1/2})^{1/2}a$ and $c = 3^{1/2}b/2$. Negative indices are represented by integers with over bars.

| Shell	Indices	Norm
M_0	[000000]	0
M_2	[110000]	b/τ
M_3	[111111]/2	c/τ^2
M_5	[1111$\bar{1}\bar{1}$]/2	τa
B_0	[000000]	0
B_3	[1$\bar{1}$1111]/2	c/τ
B_5	[100000]	$a (= 1.902\ell)$
b-linkage	[11001$\bar{1}$]	$b (= 5.236\ell)$
c-linkage	[111000]	$c (= 4.535\ell)$
$\mathbf{R}_1$	[604$\bar{4}$6$\bar{0}$]	$2b\tau^2$
$\mathbf{R}_2$	[4600$\bar{4}$6]	$2b\tau^2$
$\mathbf{R}_3$	[046$\bar{6}$04]	$2b\tau^2$

Table 3
Centres of the clusters within the unit cell extracted from the refined parameters (Appendix B).

The relevant node types (Henley, 1991) in the canonical cell tiling (§4.3) are given in the last column.

Site symbol	Atom	Wyckoff	Indices	Node type
$B_0^{(1)}$	Pd1	8c	[111000]	$(67)_{333}$
$B_0^{(2)}$	Pd6	8c	[444$\bar{1}\bar{1}\bar{1}$]	$(67)_{333}$
$B_0^{(3)}$	Pd11	24d	[33200$\bar{1}$]	$(66)_{4322}$
$B_0^{(4)}$	Pd24	24d	[44300$\bar{2}$]	$(67)_{333}$
$B_0^{(5)}$	Pd37	24d	[312$\bar{1}$20]	$(76)_{433}$
$B_0^{(6)}$	Pd50	24d	[423$\bar{1}$2$\bar{1}$]	$(76)_{433}$
$B_0^{(7)}$	Pd63	24d	[5331$\bar{1}$2]	$(67)_{333}$
$M_0^{(1)}$	Cr/Al76	4a	[000000]	$(68)_0$
$M_0^{(2)}$	Cr/Al79	4b	[3022$\bar{3}$0]	$(68)_0$
$M_0^{(3)}$	Fe/Pd82	24d	[43210$\bar{2}$]	$(57)_{3322}$
$M_0^{(4)}$	Fe/Pd90	24d	[4122$\bar{2}$1]	$(57)_{332}$
$M_0^{(5)}$	Cr/Al98	24d	[22100$\bar{1}$]	$(66)'_{432}$
$M_0^{(6)}$	Fe/Pd105	24d	[45102$\bar{4}$]	$(67)_{333}$
$M_0^{(7)}$	Fe113	24d	[4330$\bar{1}\bar{1}$]	$(67)_{333}$

central site of a cluster template as the origin, the position vector $\mathbf{x}$ of every site within the cluster template is written as $\mathbf{x} = \sum_j c_j \mathbf{a}_j =: [c_1 c_2 c_3 c_4 c_5 c_6]$, in which the indices c_j ($j = 1, 2, \ldots, 6$) are all integers or half-integers. To be more specific, each of the shells, M_x and B_x ($x = 0, 2, 3$ or 5), is the orbit of a representative member under the action of the point group $\bar{5}32/m$ (I_h); the representative indices and the radius are listed in Table 2.

4.2. Packing geometry

In the refined structure (Appendix B), the unit cell accommodates a total of 264 clusters, which divide into 128 M- and 136 B-clusters. In Table 3, the independent positions of the cluster centres are summarized. The centres of the M-clusters (M_0) are occupied mainly by Fe or Cr, although a better fit is attained if some of them are partially occupied by Pd or Al. The centres of the B-clusters (B_0) are purely occupied by Pd.

Adjacent clusters are mutually connected either along a twofold or a threefold axis with a distance of about 7.7 or 6.7 Å, respectively; these are the shortest two distances between cluster centres. An analogous feature, with the distances being τ times larger, has been extensively discussed in the case of P-type icosahedral quasicrystals and their approximants (Henley, 1986, 1991; Mihalkovic et al., 1996), in which only a single kind of cluster would come into play. The two- and threefold linkages are called b- and c-linkages, respectively, whereas a packing of clusters with this property is called a bc-packing. The b- and c-linkages are indexed with integers and their representatives are given in Table 2; the respective norms are denoted b and c ($= 3^{1/2}b/2$). The skeleton of the crystal structure can thus be described as a network of nodes, which correspond to the cluster centres, connected through b- and c-linkages.

F-type ordering (or F-centring) in icosahedral quasicrystals as well as their approximants occurs as the even and odd parities of the nodes in the relevant bc-packing are differ-

entiated. Here, the parity of each node is defined as that of the sum of the relevant indices. Note in Table 2 that each b-linkage connects a pair of nodes having the same parity, while each c-linkage connects a pair of nodes having different parities. Therefore, if the two kinds of cluster, M and B, are the entities that differentiate the two subsets of the nodes of a bc-packing, it follows that every b-linkage connects the same kind of cluster (M–M or B–B), while every c-linkage connects different kinds of cluster (M–B). The three combinations for an adjacent pair of clusters are depicted in Fig. 6.

The coordinates of the cluster centres given in the refined atomic parameters (Appendix B) can be used to enumerate which of the b- and c-linkages connect every node to its adjacent neighbours. The task of obtaining the indices for every cluster centre is straightforward. First we set the indices of the atomic site Cr/Al76 lying at the origin $(0, 0, 0)$, which is the centre of an M-cluster, to [000000]. Then we recursively
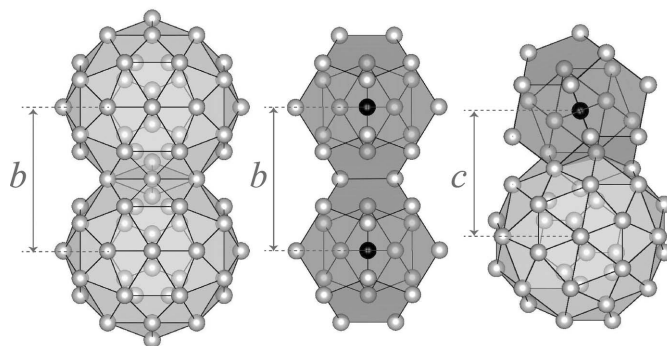
Figure 6
The three different combinations for an adjacent pair of clusters: M–M (left), B–B (middle) and M–B (right). Two clusters of the same kind are connected via a b-linkage, while those of the two different kinds are connected via a c-linkage. The sites in the constituent cluster templates are depicted as spheres. The drawing plane is perpendicular to a twofold symmetry axis.

trace linkages to obtain the indices of adjacent cluster centres until all the cluster centres within the unit cell as well as the lattice translation vectors are identified. The resulting lattice translation vectors $\mathbf{R}_j$ ($j = 1, 2$ and 3) are presented in Table 2. Since the lattice constant $|\mathbf{R}_j| = 2b\tau^2$ should equal the experimental value of $a_{lat} = 40.54$ Å, the basic parameter b is immediately evaluated as 7.74 Å.

Now we are equipped with the proper scale for examining the interatomic distances. Let us first note that the ideal edge length b/τ^3 of the inner dodecahedral shell of an M-cluster (M_3; Fig. 5a) is evaluated to be 1.83 Å and that it is unrealistically short for an interatomic distance. A natural consequence of this is that the relevant shells cannot be occupied by more than eight atoms simultaneously. Next, note that the outer shell of an M-cluster (including the two subshells) has two kinds of edges. The edges connecting the adjacent pairs in the M_2 subshell are parallel to the twofold axes and have a length of $b' := b/\tau^2 = 2.958$ Å, while those connecting the M_2 subshell with the M_5 subshell are parallel to the threefold axes and have a length of $c' := c/\tau^2 = 2.562$ Å. The latter two edge lengths are reasonable for interatomic distances. Similarly, the edges connecting the adjacent pairs in the inner (B_5) or the outer (B_3) shell of a B-cluster are parallel to the twofold axes and have a length of b'. Interestingly, the two kinds of linkages, namely b' and c', form the majority of the interatomic linkages in the idealized construction. This applies not only to the closest interatomic linkages within each shell of a cluster but also to those connecting between the inner and the outer shells. It follows that the closest distances are b' for the pairs M_3–M_3, M_2–M_2, M_3–M_5, B_5–B_5 and B_3–B_3, and c' for the pairs M_2–M_5, M_3–M_2 and B_5–B_3. Here we have included the pair M_3–M_3 because the closest interatomic distance that is allowed within the partially occupied inner shell (M_3) of an M-cluster is b'.

Two M-clusters connected through a b-linkage interpenetrate into each other (Fig. 6, left) with the overlap between the outer polyhedra being a flat hexagonal bipyramid. The two tips of the bipyramid belong to the M_2 shells and are very close to each other (1.828 Å), so that they cannot be occupied simultaneously. In the refinement, such positions have been well fitted as splitting positions for a single Al atom. The intersection between the two M-clusters consists of the six sites forming the base hexagon of the hexagonal bipyramid; two of them belong to the M_5 subshells of the two M-clusters while the remaining four belong to the M_2 subshells. On the other hand, two B-clusters connected through a b-linkage share an edge between their outer shells (B_3, Fig. 6, middle). In both cases, the intersection between the two clusters does not involve the inner shells.

The situation is somewhat more intricate in the case of an M–B pair connected through a c-linkage. Observe in Fig. 6 (right) that the outer shell (B_3) of the B-cluster penetrates to the inner shell (M_3) of the M-cluster, where a site is shared between these shells. Similarly, the outer subshell (M_2) of the M-cluster penetrates to the inner shell (B_5) of the B-cluster, where a triangular face is shared between these shells. One also finds that these clusters intersect with each other in their

outer (sub)shells M_5 and B_3, too, where there are three common sites between the two.

The idealized atomic positions can be obtained by replicating the relevant cluster templates at the positions given in Table 3. The arrangement of clusters in a unit cell is illustrated in Fig. 7. As we have just seen, an atomic position can belong to two or more cluster shells that intersect with each other. Therefore, each individual site can be characterized by the set of cluster shells to which it belongs. Take, for instance, a site in the inner shell (M_3) of an M-cluster belonging also to the outer shell (B_3) of an adjacent B-cluster. We simply assign to this site a class, $\langle M_3, B_3 \rangle$. More generally, if an atomic site belongs to n cluster shells, $X^1, X^2, \ldots, X^n$, then the class associated with this site would be $\langle X^1, X^2, \ldots, X^n \rangle$. Bear in mind that only the combination of the cluster shells matters here, so that the order of the shell symbols in the angle brackets is irrelevant. It turns out that the idealized structure of the present crystal contains in total 16 different classes of atomic sites, which are listed in Table 4.

It is obvious from the above argument that the central site of each cluster cannot be shared by any other cluster. Hence, the symbols for the cluster centres are $\langle M_0 \rangle$ and $\langle B_0 \rangle$. In addition, the crystal structure includes three more classes of unshared sites, which are $\langle M_2 \rangle$, $\langle M_3 \rangle$ and $\langle B_5 \rangle$. Importantly, the former two bear distinct roles in the physical construction of the structure: (i) $\langle M_2 \rangle$, the splitting positions given at the tip of the overlap hexagonal bipyramid associated with each interpenetrating pair of M-clusters and (ii) $\langle M_3 \rangle$, the vacant sites in the M_3 shells of the M-clusters. Remember that the inner shell of an M-cluster (M_3) cannot accommodate more than eight atoms owing to the constraint imposed by the short nearest-
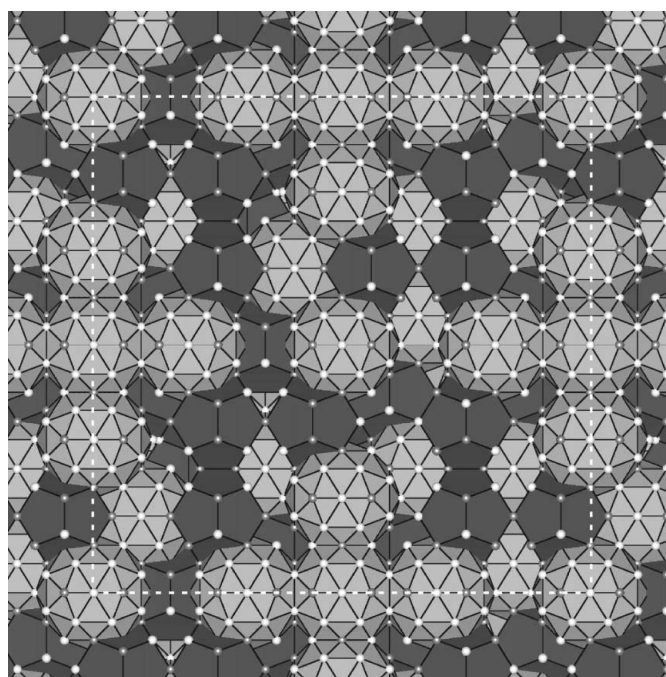
Figure 7
The packing of clusters. The square drawn with white dashed lines indicates a face of the cubic unit cell, whereas the horizontal and vertical edges correspond to the primitive lattice vectors, $\mathbf{R}_1$ and $\mathbf{R}_2$, respectively.

Table 4
The 16 different classes of idealized atomic sites.

Their number frequencies per unit cell, presented in the second column, sum up to a total of 4680. The average composition (in percentage) of each class is given in the last column, where 'Vc' stands for vacancy.

Site class	Number	Average composition
$\langle M_0 \rangle$	128 (= F)	$Al_6Pd_4(Cr,Fe)_{90}$
$\langle M_2 \rangle$	720 (= G)	$Al_{50}Vc_{50}$
$\langle M_3 \rangle$	1680 (= H)	Vc_{100}
$\langle B_0 \rangle$	136 (= I)	Pd_{100}
$\langle B_5 \rangle$	24 (= J)	Al_{100}
$\langle M_2, M_2 \rangle$	72 (= K)	Al_{100}
$\langle M_2, B_5 \rangle$	576 (= L)	Al_{100}
$\langle M_3, B_3 \rangle$	880 (= M)	$Al_{81}Pd_1(Cr,Fe)_{17}Vc_1$
$\langle M_5, B_3 \rangle$	24 (= N)	Pd_{100}
$\langle B_3, B_3 \rangle$	72 (= O)	Pd_{100}
$\langle M_2, M_2, B_5 \rangle$	1032 (= P)	Al_{100}
$\langle M_2, M_2, M_2 \rangle$	112 (= Q)	Al_{100}
$\langle M_5, M_5, M_5 \rangle$	24 (= R)	$Al_1(Cr,Fe)_{99}$
$\langle M_5, B_3, B_3 \rangle$	408 (= S)	$Pd_{98}(Cr,Fe)_2$
$\langle M_5, M_5, B_3, B_3 \rangle$	384 (= T)	$Pd_{65}(Cr,Fe)_{35}$
$\langle M_5, M_5, M_5, B_3 \rangle$	88 (= U)	$Pd_3(Cr,Fe)_{97}$

neighbour distance. And it is clearly demonstrated by our structure analysis that the only occupied M_3 sites are those represented by the symbol $\langle M_3, B_3 \rangle$. The last unshared class $\langle B_5 \rangle$ does not seem to differ from the other types of B_5 sites, as all of them are fully occupied by Al.

Correlations are further found between the local compositions at individual atomic sites and the site classes. Take, for instance, the B_3 shell, which involves six different site classes (Table 4). Whereas the sites symbolized as $\langle M_3, B_3 \rangle$ are primarily occupied by Al, the sites in the remaining five classes, $\langle M_5, B_3 \rangle$, $\langle B_3, B_3 \rangle$, $\langle M_5, B_3, B_3 \rangle$, $\langle M_5, M_5, B_3, B_3 \rangle$ and $\langle M_5, M_5, M_5, B_3 \rangle$, are occupied by markedly heavier elements in different degrees. Similar observations suggest that the physical nature of an individual atomic site is profoundly affected by the manner in which the clusters intersect there. Therefore, the two kinds of clusters not only provide a handy means of describing the complex structure but also serve as the true physical units that play a significant role in the formation of the structure. This underlying basic idea may also apply to a more general class of Al-based alloys which exhibit F-type icosahedral ordering.

The packing of the cluster templates as described above generates in total 4680 idealized atomic positions (excluding the vacant $\langle M_3 \rangle$ sites), which agree remarkably well with the refined atomic positions, although in the refinement we included 48 additional sites which are needed to explain minor irregularities in the real material. Importantly, the gaps between the clusters are small enough and do not accommodate any additional atoms (called glue atoms). In §5.3, this feature is described from a somewhat different viewpoint.

4.3. Canonical cell tiling with F-type ordering

The skeletal structure of the present approximant is described as the *bc*-packing, in which the cluster centres are represented as the nodes (Table 3). The nodes can be connected to each other through edges of two kinds (*b*- and *c*-

linkages; Fig. 8a), whereas the edges form three kinds of polygons: an isosceles triangle formed by a *b*-linkage and two *c*-linkages (X-face; point symmetry *m*), an equilateral triangle formed by three *b*-linkages (Y-face; 3*m*) and a rectangle formed by two *b*-linkages and two *c*-linkages (Z-face; 2/*m*) (Fig. 8b). These polygons are further found to be the faces of four kinds of polyhedra called the *canonical cells* (Henley, 1991): a tetrahedron with four X-faces (A-cell; 2*m*), a pyramid with three X-faces, one Y-face and one Z-face (B-cell; *m*), a tetrahedron with three X-faces and one Y-face (C-cell; 3*m*), and a trigonal prism with two Y-faces and three Z-faces (D-cell; 3*m*) (Fig. 8c). The present *bc*-packing thus proves to be represented as a periodic tiling of space called a canonical cell tiling (CCT); that is, the whole space is divided into pieces congruent to the canonical cells (Fig. 9).
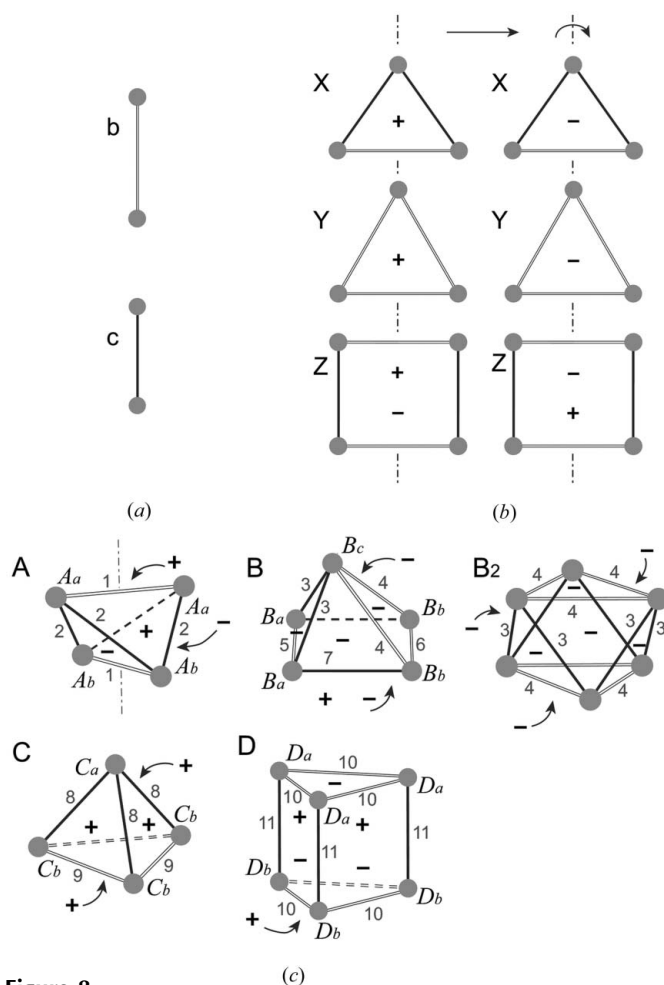
Figure 8
The canonical cells and their geometrical components. (a) The two kinds of linkages, *b* and *c*, represented as double and thick bars, respectively. (b) The three kinds of faces, X, Y and Z, whose sides are distinguishable in terms of the icosahedral symmetry; where the '+' sign is on one side, the '−' sign is on the other side. The reverse sides of the faces are shown by rotating them by 180° around the vertical dashed line. (c) The four canonical cells, A, B, C and D, and a trigonal anti-prism unit, B_2, which can be divided into two B-cells in three ways. The unique corners are indicated by the corner symbols, while the numbers on the edges correspond to the following dihedral angles: (1) $\pi/2$, (2) $\pi/3$, (3) $\pi - \varepsilon$, (4) $\pi - \eta$, (5) η, (6) $\pi - 2\eta$, (7) $(\pi - \varepsilon)/2$, (8) ε, (9) η, (10) $\pi/2$ and (11) $\pi/3$.

The decoration of CCTs with atoms has been considered to be a promising route to model the atomic structure of P-type icosahedral quasicrystals and their approximants (Henley, 1991; Mihalkovic *et al.*, 1996). For Al-based P-type icosahedral quasicrystals, *e.g.* i-AlMn, canonical cells with edge lengths of $b = 12.7$ and $c = 11.0$ Å are typically assumed. On the other hand, the present compound demonstrates for the first time that the CCT construction extends naturally to approximant phases to F-type icosahedral quasicrystals. However, important differences are found here. Firstly, the two parities of the nodes need to be distinguished to account for the F-type ordering as illustrated by the colouring of the nodes in Fig. 9. Secondly, the sizes of the cells are approximately $1/\tau$ times those in the conventional description ($b = 7.74$ and $c = 6.70$ Å), which also implies the sizes of the relevant clusters are much smaller.

The geometrical composition of the present CCT is summarized in Table 5. There are 11 congruence classes of objects, some of which are further divided into two subclasses (I and II) owing to the parities of the nodes, leading to 18 object classes in total. Remember that an X-face as well as an A-, B-, C- or D-cell has more than one unique corner (see the corner symbols in Table 5), for which the parities need to be specified explicitly. It follows that there are two ways of colouring the vertices of each kind of cell, leading to two different configurations of clusters and thus to two different
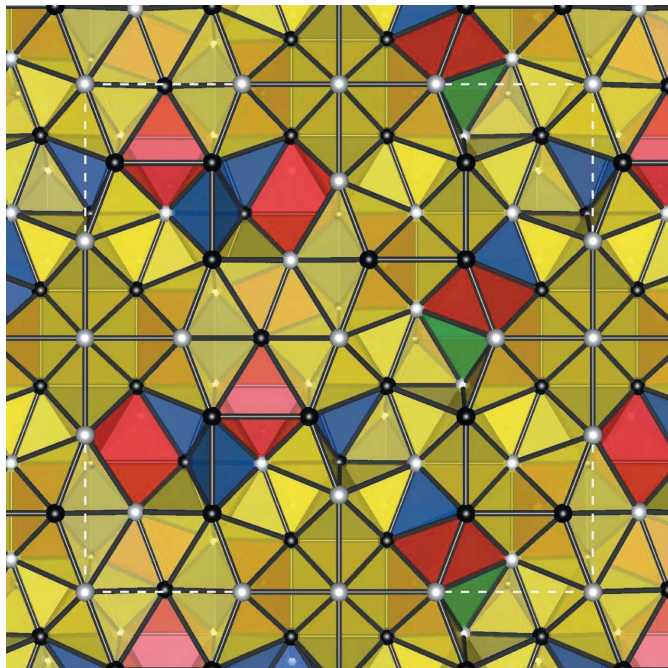
Figure 9
A top view of a cleaved surface of the present CCT parallel to the (001) plane; the foremost cells are chosen somewhat arbitrarily. The spheres representing the even (respectively, odd) nodes are coloured white (respectively, black). The white dashed lines indicate a square face of the cubic unit cell, while the horizontal and vertical edges correspond to the primitive lattice vectors, $\mathbf{R}_1$ and $\mathbf{R}_2$, respectively. At the lower left corner of the square lies an even node corresponding to the origin. The four kinds of canonical cells are coloured yellow (A-cell), red (B-cell), blue (C-cell) and green (D-cell).

Table 5
The number frequencies of the geometrical objects contained in a single unit cell of the present CCT.

The 11 congruent types can be further divided into subclasses according to the parities of the nodes as specified in the parentheses using the symbols + (for even) and − (for odd), leading to 18 basic object types. Note that for the faces (X–Z) as well as the cells (A–D), the parity symbols are arranged in the same order as the corner symbols referenced in the second column. The object type B_2 can be divided into two B-cells in three different ways, and we do not take it as a basic object type.

Object	Type (I)	(II)
Node	128 (+)	136 (−)
Edge b	360 (+ +)	432 (− −)
Edge c	* 880 (+ −)	
Face X ($X_a X_a X_b$)	1032 (+ + −)	1176 (− − +)
Face Y ($Y_a Y_a Y_a$)	112 (+ + +)	176 (− − −)
Face Z ($Z_a Z_a Z_a Z_a$)	* 176 (+ + − −)	
Cell A ($A_a A_a A_b A_b$)	384 (+ + − −)	336 (− − + +)
Cell B ($B_a B_a B_b B_b B_c$)	104 (− − + + +)	152 (+ + − − −)
Cell B_2 ($B_c B_c B_c B_c B_c B_c$)	* 80 (+ + + − − −)	
Cell C ($C_a C_b C_b C_b$)	88 (− + + +)	168 (+ − − −)
Cell D ($D_a D_a D_a D_b D_b D_b$)	8 (+ + + − − −)	24 (− − − + + +)

atomic arrangements within the cell (in the sense that the atomic species are disregarded).

The present argument extends naturally to arbitrary CCTs, whereby a number of hypothetical approximants with F-type ordering can be constructed. From this perspective, it is worthwhile making a general consideration on the statistics of the geometrical objects as well as that of the atomic sites. However, if the reader prefers not to delve into the mathematical derivations for the moment, the rest of this subsection can be safely skipped.

In the following argument, the number density of an arbitrary object type O among the 18 basic object types is denoted $n(O)$. In particular, the number densities of the eight types of cells are of fundamental importance, so that we introduce the following parameters: $\alpha_I = n(A_I)$, $\alpha_{II} = n(A_{II})$, $\beta_I = n(B_I)$, $\beta_{II} = n(B_{II})$, $\gamma_I = n(C_I)$, $\gamma_{II} = n(C_{II})$, $\delta_I = n(D_I)$ and $\delta_{II} = n(D_{II})$. The following sums are also used whenever it is convenient to do so:

$$\alpha := \alpha_I + \alpha_{II}, \quad \beta := \beta_I + \beta_{II},$$
$$\gamma := \gamma_I + \gamma_{II}, \quad \delta := \delta_I + \delta_{II}. \tag{2}$$

By definition, the sum rule for the cell volumes is written as

$$v_A \alpha + v_B \beta + v_C \gamma + v_D \delta = 1, \tag{3}$$

where $v_A = b^3/12$, $v_B = 5^{1/2} b^3/12$, $v_C = 5^{1/2} b^3/24$ and $v_D = 3b^3/8$ are the volumes of the A-, B-, C- and D-cells, respectively. In addition to this, these statistical parameters hold a set of universal equations due to geometrical constraints imposed by the shapes of the cells.

Let us first consider the matching constraints across the faces. Take, for instance, a cell that has an X_I face with its + side facing outward, then another cell with an X_I face with its − side facing outward can only match the former cell. Since the same requirement is fulfilled across any of the X_I faces in

the structure, the + and − sides of the faces of this type must appear an equal number of times. By counting the two distinct sides of X_I faces for each type of cell, equation (4) can be readily verified. Furthermore, similar considerations when applied to the X_{II}, Y_I and Y_{II} faces lead to equations (5), (6) and (7), respectively.

$$2\alpha_I + 3\gamma_I = 2\alpha_{II} + 2\beta_I + \beta_{II}, \tag{4}$$

$$2\alpha_{II} + 3\gamma_{II} = 2\alpha_I + 2\beta_{II} + \beta_I, \tag{5}$$

$$\beta_I + \delta_I = \gamma_I + \delta_{II}, \tag{6}$$

$$\beta_{II} + \delta_{II} = \gamma_{II} + \delta_I. \tag{7}$$

Now we show that the matching constraints around the edges will lead to two more equations. Note that the dihedral angles contained in a B- or C-cell (see Fig. 8c) involve two irrational constants, ε and η, defined by (Henley, 1991)

$$\varepsilon \equiv \arccos{(1/4)} \simeq 4\pi(0.1049), \tag{8}$$

$$\eta \equiv \arccos{(1/6^{1/2})} \simeq 4\pi(0.0915). \tag{9}$$

Here each cell contributes a fixed amount of dihedral angles associated with a fixed edge type. Hence, the contributions from all the cells sum up to the total number of the relevant edges times 2π; that is,

$$2\pi n(b_I) = (\pi/2)\alpha + (3\pi - 4\eta)\beta_I + \eta\beta_{II} + 3\eta\gamma_I + (3\pi/2)\delta, \tag{10}$$

$$2\pi n(b_{II}) = (\pi/2)\alpha + \eta\beta_I + (3\pi - 4\eta)\beta_{II} + 3\eta\gamma_{II} + (3\pi/2)\delta, \tag{11}$$

$$2\pi n(c) = (4\pi/3)\alpha + 3(\pi - \varepsilon)\beta + 3\varepsilon\gamma + \pi\delta. \tag{12}$$

Observe that in equations (10)–(12) terms containing ε and η do not cancel out spontaneously. Hence, in order to avoid unphysical consequences, that is the number of edges of each type would be irrational, we need to constrain the coefficients for ε and η to be zero. Therefore, the following equations need to be satisfied:

$$-4\beta_I + \beta_{II} + 3\gamma_I = 0, \quad \beta_I - 4\beta_{II} + 3\gamma_{II} = 0,$$
$$-3\beta + 3\gamma = 0. \tag{13}$$

One can readily check that equations (4)–(7) and (13) can be reduced to the following four universal equations:

$$\beta = \gamma, \quad \Delta\alpha = -\Delta\beta,$$
$$3\Delta\gamma = 5\Delta\beta, \quad 3\Delta\delta = \Delta\beta, \tag{14}$$

where

$$\Delta\alpha := \alpha_I - \alpha_{II}, \quad \Delta\beta := \beta_I - \beta_{II},$$
$$\Delta\gamma := \gamma_I - \gamma_{II}, \quad \Delta\delta := \delta_I - \delta_{II}. \tag{15}$$

It follows from equations (3) and (14) that there are only three independent degrees of freedom to determine the statistical properties of any CCT with F-type ordering. Following Henley (1991), an independent parameter μ is defined as the volume fraction occupied by A- and D-cells:

$$\mu := \nu_A\alpha + \nu_D\delta, \tag{16}$$

while another ζ is defined so that $\mu\zeta$ gives the volume fraction occupied by D-cells:

$$\zeta := \nu_D\delta/\mu. \tag{17}$$

It is readily shown that these two parameters determine the number densities of the canonical cells through (Henley, 1991)

$$\alpha = 12\mu(1 - \zeta)/b^3, \tag{18}$$

$$\beta \equiv \gamma = (8/5^{1/2})(1 - \mu)/b^3, \tag{19}$$

$$\delta = (8/3)\mu\zeta/b^3. \tag{20}$$

The last independent parameter ν, which is necessary if F-type ordering is considered, can be defined as

$$\nu := \Delta\beta/\beta. \tag{21}$$

As soon as the statistics are fixed for the cells, it is a straightforward task to enumerate the objects of lower dimensionalities (faces, edges and nodes) by taking the contributions from all the cells. The edges have already been enumerated via equations (10)–(12), while for enumerating the faces the double counting of each face must be taken care of. The nodes are enumerated by taking the sum of the solid angles associated with the relevant corners of the cells (Henley, 1991) and by dividing the results by 4π. The resulting formulae are

$$n(\text{node}_I) = \alpha/12 + \beta/4 + \Delta\beta/12 + \delta/4, \tag{22}$$

$$n(\text{node}_{II}) = \alpha/12 + \beta/4 - \Delta\beta/12 + \delta/4, \tag{23}$$

$$n(b_I) = \alpha/4 + 3(\beta + \Delta\beta)/4 + 3\delta/4, \tag{24}$$

$$n(b_{II}) = \alpha/4 + 3(\beta - \Delta\beta)/4 + 3\delta/4, \tag{25}$$

$$n(c) = 2\alpha/3 + 3\beta/2 + \delta/2, \tag{26}$$

$$n(X_I) = \alpha + 3(\beta + \Delta\beta)/2, \tag{27}$$

$$n(X_{II}) = \alpha + 3(\beta - \Delta\beta)/2, \tag{28}$$

$$n(Y_I) = \beta/2 + 2\Delta\beta/3 + \delta/2, \tag{29}$$

$$n(Y_{II}) = \beta/2 - 2\Delta\beta/3 + \delta/2, \tag{30}$$

$$n(Z) = (\beta + 3\delta)/2. \tag{31}$$

The numbers of objects listed in Table 5 are the frequencies within a single unit cell. These values can be readily compared with the above formulae by re-interpreting the variables as the frequencies per unit cell, that is, $\alpha\Omega = 720$, $\beta\Omega = 256$, $\Delta\beta\Omega = -48$ and $\delta\Omega = 32$.

Each of the above 18 object types offers a possible local atomic configuration through replicating the relevant cluster templates. Therefore, the above statistics uniquely determine the number densities $f = F/\Omega, g = G/\Omega, \ldots, u = U/\Omega$ of the 16 types of atomic sites; see Table 4. One can readily prove the following general formulae (see Appendix A):

$$f = \alpha/12 + \beta/4 + \Delta\beta/12 + \delta/4, \tag{32}$$

$$g = \alpha/2 + 3\beta/2 + 3\Delta\beta/2 + 3\delta/2, \tag{33}$$

$$h = \alpha + 7\beta/2 + 5\Delta\beta/3 + 9\delta/2, \tag{34}$$

$$i = \alpha/12 + \beta/4 - \Delta\beta/12 + \delta/4, \tag{35}$$

$$j = \Delta\beta/2 + 3\delta/2, \tag{36}$$

$$k = -\Delta\beta/2 + 3\delta/2, \tag{37}$$

$$l = 3\beta/2 - 3\Delta\beta + 3\delta/2, \tag{38}$$

$$m = 2\alpha/3 + 3\beta/2 + \delta/2, \tag{39}$$

$$n = \Delta\beta/2 + 3\delta/2, \tag{40}$$

$$o = -\Delta\beta/2 + 3\delta/2, \tag{41}$$

$$p = \alpha + 3\beta/2 + 3\Delta\beta/2, \tag{42}$$

$$q = \beta/2 + 2\Delta\beta/3 + \delta/2, \tag{43}$$

$$r = -\Delta\beta/6 + \delta/2, \tag{44}$$

$$s = 3\beta/2 - \Delta\beta/2, \tag{45}$$

$$t = \alpha/2 - \Delta\beta/2, \tag{46}$$

$$u = \beta/2 + 5\Delta\beta/6. \tag{47}$$

Remembering that each individual site exhibits a chemical composition that is substantially correlated with the site class, the derived statistics could be useful when estimating the chemical composition of a hypothetical crystal that is derived from a CCT. This may facilitate an experimental search for unknown approximants in closely related alloy systems.

5. Discussion

The new model presented in §4 allows a concise description of the extremely complex material, offering the possibility that the stabilization mechanisms as well as the physical properties will be clarified on a structural basis. In particular, the model will lead us to revised views on bondings, defects and dynamics in related materials. At present, our model cannot be extended naively to icosahedral quasicrystals because there is currently no proof as to whether a CCT (Henley, 1991) can be made such that it has quasiperiodicity as well as icosahedral symmetry.[3] One can nevertheless gain an important insight into the quasicrystalline state by evaluating how close (or how far) the given crystal lies to (or from) an idealized quasicrystal.

---

[3] Computational techniques for generating CCTs with large periods have been developed by several authors (Mihalkovic & Mrafko, 1993; Newman *et al.*, 1995). These techniques search possible arrangements of canonical cells under preset periodic boundary conditions, where the amount of computations will expand exponentially as the periods are increased. There is no way that the preset periods can be extrapolated to infinity; hence, it still remains a challenge to verify the existence of quasiperiodic CCTs.

The following subsections are devoted to discussions on some of these topics.

5.1. Superlattice ordering

In the standard six-dimensional formalism for icosahedral quasicrystals, the three-dimensional physical space $\mathbb{E}$ is thought of as a subspace of a six-dimensional hyperspace $\tilde{\mathbb{E}}$, whereas the orthogonal complement to the physical space is called the perpendicular space $\mathbb{E}_\perp$. The hyperspace is the direct sum of the two subspaces; that is, $\tilde{\mathbb{E}} = \mathbb{E} \oplus \mathbb{E}_\perp$. Accordingly the basis vectors $\mathbf{a}_j$ ($\in \mathbb{E}$) defined in equation (1) are lifted into six dimensions *via* $\tilde{\mathbf{a}}_j = (\mathbf{a}_j, c\mathbf{a}_j^\perp)$, where c ($\in \mathbb{R}$) is an arbitrary non-zero factor and $\mathbf{a}_j^\perp$ ($\in \mathbb{E}_\perp$) are defined by

$$(\mathbf{a}_1^\perp \ \mathbf{a}_2^\perp \ \mathbf{a}_3^\perp \ \mathbf{a}_4^\perp \ \mathbf{a}_5^\perp \ \mathbf{a}_6^\perp)$$
$$:= \ell \begin{pmatrix} 1 & 0 & -\tau & -\tau & -1 & 0 \\ -\tau & 1 & 0 & 0 & -\tau & -1 \\ 0 & -\tau & 1 & -1 & 0 & -\tau \end{pmatrix}. \tag{48}$$

If c is taken to be unity, the six-dimensional basis vectors $\tilde{\mathbf{a}}_j$ ($\in \tilde{\mathbb{E}}$) form an orthogonal basis set that generates a six-dimensional hyper-cubic lattice, $\tilde{\mathbb{L}}_P$, where the subscript P stands for the primitive lattice (P-type). The norm of the six-dimensional basis vectors is hereafter denoted $\tilde{a}$ ($:= |\tilde{\mathbf{a}}_j| = 2^{1/2}a$), which is evaluated to be 3.977 Å from the present approximant.

Provided that we have a structure in which the arrangement of M- and B-clusters is subject to the local rules presented in §4.2, each cluster is centred at a position that is represented as

$$\mathbf{x} = n_1\mathbf{a}_1 + n_2\mathbf{a}_2 + n_3\mathbf{a}_3 + n_4\mathbf{a}_4 + n_5\mathbf{a}_5 + n_6\mathbf{a}_6$$
$$=: [n_1n_2n_3n_4n_5n_6], \tag{49}$$

where n_j ($j = 1, 2, \ldots, 6$) are the indices, namely, the integer coefficients that are determined uniquely if the origin is taken at one of the cluster centres. The kind of cluster (respectively, M or B) depends on the parity of $\mathbf{x}$ (respectively, even or odd), where the parity is defined as that of the sum $\sum_j = n_j$.

The three-dimensional vector $\mathbf{x}$ can be lifted to a six-dimensional counterpart $\tilde{\mathbf{x}} \in \tilde{\mathbb{L}}_P$ simply by replacing $\mathbf{a}_j$ in equation (49) with $\tilde{\mathbf{a}}_j$. Then, $\mathbf{x}$ is the image of $\tilde{\mathbf{x}}$ through the orthogonal projection of $\tilde{\mathbb{E}}$ onto $\mathbb{E}$. The image $\mathbf{x}^\perp$ of $\tilde{\mathbf{x}}$ in $\mathbb{E}_\perp$ is definable in a similar way. It is readily understood that the three-dimensional vectors $\mathbf{x}$ and $\mathbf{x}^\perp$ maintain a one-to-one correspondence (bijection) with each other, where $\mathbf{x}^\perp$ is called the conjugate image of $\mathbf{x}$. The parities of $\mathbf{x}$, $\mathbf{x}^\perp$ and $\tilde{\mathbf{x}}$ are equal. The even subset (consisting of the vertices of even parity) in $\tilde{\mathbb{L}}_P$ forms a sublattice with an index of 2 and it gives an F-type (or F-centred) hyper-cubic lattice $\tilde{\mathbb{L}}_F$, having a lattice constant of $\tilde{a}_F := 2\tilde{a}$.

The perfect icosahedral symmetry of an ideal quasicrystal requires that the conjugate images of all the cluster centres be bounded within a finite domain $\mathbb{W}$ ($\subset \mathbb{E}_\perp$) called a window, which is also called an atomic surface or an acceptance domain. If this is the case, the lifted coordinates $\tilde{\mathbf{x}}$ are distributed along the three-dimensional cut space $\mathbb{E} + \mathbf{w}_0$ in $\tilde{\mathbb{E}}$, where $\mathbf{w}_0$($\in \mathbb{E}_\perp$) is the centre of mass of the window. This can

be put also as $\mathbf{x}^{\perp} \sim \mathbf{w}_0$, which is a loose but useful expression in a context where the deviation from equality is unimportant.

If the cut space is taken to be inclined linearly against $\mathbb{E}$, the coordinates of the cluster centres would behave as $\mathbf{x}^{\perp} \sim \mathbf{A} \cdot \mathbf{x} + \mathbf{w}_0$, in which $\mathbf{A}$ is a 3×3 matrix called the linear phason tensor. An approximant in particular has a cut space that is parallel to one of the lattice planes of $\tilde{\mathbb{L}}_{\mathrm{P}}$, such that any lattice translation vector $\mathbf{R}$ for the approximant satisfies $\mathbf{R}^{\perp} = \mathbf{A} \cdot \mathbf{R}$, where $\mathbf{R}^{\perp}$ is the conjugate image of $\mathbf{R}$. Therefore, the task of evaluating $\mathbf{A}$ for the present approximant can resort to the primitive lattice translation vectors given in Table 2, reading

$$\mathbf{A} = \left(\mathbf{R}_1^{\perp}\, \mathbf{R}_2^{\perp}\, \mathbf{R}_3^{\perp} \right) \left(\mathbf{R}_1\, \mathbf{R}_2\, \mathbf{R}_3 \right)^{-1}$$
$$= \frac{29 - 13(5)^{1/2}}{2} \mathbf{I} = -\tau^{-7} \mathbf{I}, \tag{50}$$

where $\mathbf{I}$ is the 3×3 identity matrix. The smallness of the linear phason strain implies that the crystal is rather close to an ideal quasicrystal.

The present approximant can indeed be identified as a $2 \times 2 \times 2$ superstructure of the cubic 3/2 approximant in the series of rational approximations to icosahedral quasicrystallinity. The cubic 3/2 approximant, which is constructed by decorating a CCT called the 3/2 packing (Henley, 1991) using the decoration rules of §4, has a lattice constant of $b\tau^2$; this hypothetical crystal structure is illustrated in Fig. 10. Observe a marked resemblance of this unit cell to each 1/8 block (half cube) cut out from the cubic unit cell of the superstructure (Fig. 7). The primitive lattice translation vectors of the
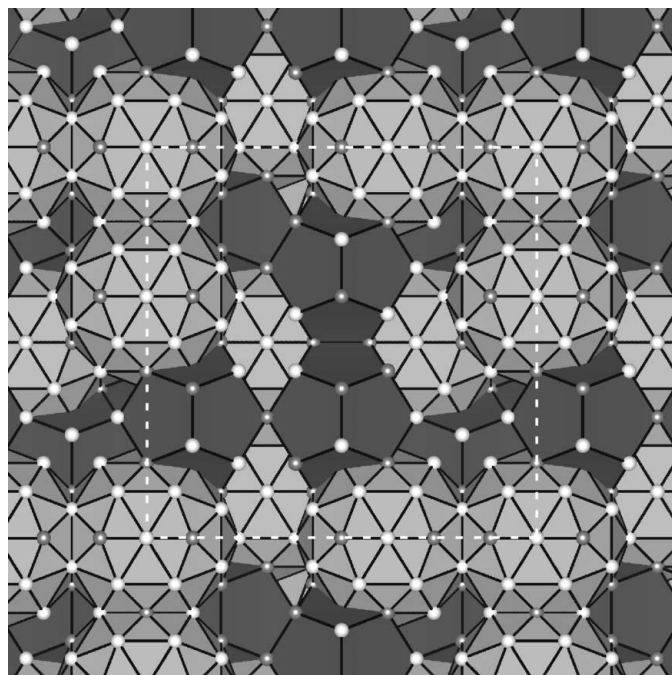
Figure 10
The packing of clusters for a hypothetical cubic 3/2 approximant. The square drawn with white dashed lines indicates a face of the cubic unit cell, whereas the horizontal and vertical edges correspond to the primitive lattice vectors, $\mathbf{R}_1' = \mathbf{R}_1/2$ and $\mathbf{R}_2' = \mathbf{R}_2/2$, respectively.

hypothetical 3/2 approximant are $\mathbf{R}_j' = \mathbf{R}_j/2$ with $j = 1$, 2 and 3. Note that the linear phason tensor is unchanged from that given in equation (50) because the corresponding indices (even numbers) for $\mathbf{R}_j$ are simply halved for $\mathbf{R}_j'$. The space group $Pa\overline{3}$ of the 3/2 packing (Henley, 1991) is reduced to $P2_13$ because the atomic decoration distinguishes the even and odd parities of the nodes. Accordingly, the hypothetical 3/2 approximant should have the enantiomorphic (or chiral) point group 23. When the superlattice ordering is induced, the space group $Pa\overline{3}$ including the centre of symmetry is restored.

It turns out that not only rearrangements of clusters but also additions of extra clusters close to the boundaries between half cubes are necessary in realizing the superstructure. The latter can be checked when the packing densities of the two structures are compared. A single unit cell of the 3/2 approximant with a volume of $b^3\tau^6$ $(=: \Omega_{3/2})$ contains 16 M- and 16 B-clusters, while that of the present superstructure with a volume of $\Omega = 8\Omega_{3/2}$ contains 128 M- and 136 B-clusters. Eight additional B-clusters (*cf.* $8 = 136 - 16 \times 8$) are included in the unit cell, causing an increase in the number density of clusters from $1.78/b^3$ to $1.84/b^3$. The present superstructure gives a relatively dense packing as compared to most of the simplest CCTs described by Henley (1991); the only two with higher densities are the cubic 1/1 and 2/1 packings with the number densities of clusters being $2/b^3$ and $1.89/b^3$, respectively.

A clear contrast between the basic skeleton of the present approximant (superstructure) and that of the 3/2 approximant can be demonstrated with their *modified* conjugate images. Generally speaking, the conjugate images of the cluster centres would be unbounded if there exists a non-zero linear phason strain, namely $\mathbf{A} \neq \mathbf{O}$ ($\mathbf{O}$, the 3×3 zero matrix), because $\mathbf{x}$ in $\mathbf{x}^{\perp} \sim \mathbf{A} \cdot \mathbf{x} + \mathbf{w}_0$ runs across the physical space $\mathbb{E}$. Hence, one needs to consider the modified conjugate images

$$\mathbf{x}_{\mathrm{mod}}^{\perp} := \mathbf{x}^{\perp} - \mathbf{A} \cdot \mathbf{x}, \tag{51}$$

which behave as $\mathbf{x}_{\mathrm{mod}}^{\perp} \sim \mathbf{w}_0$. In Fig. 11, the modified conjugate images of the nodes of the two skeletons are depicted as white and black spheres, which correspond to the centres of M- and B-clusters, respectively. The truncated octahedron $\mathscr{O}$ depicted in each panel (centred at the centre of mass of the modified conjugate images of the nodes) represents the modified window associated with the 3/2 packing. All the vertices and the hexagonal face centres of $\mathscr{O}$ are obtained as the modified versions [*via* equation (51)] of the 32 vertices of a rhombic triacontahedron $\mathscr{C}_{12}$ $(\subset \mathbb{E}_{\perp})$, which is the window for the 12-fold vertices in the three-dimensional Penrose tiling; for the definition of $\mathscr{C}_{12}$, refer to the original article (Henley, 1986) and Fig. 9(*a*) therein. We find in Fig. 11 (left) that the modified conjugate images of the nodes in the 3/2 packing are well confined within $\mathscr{O}$, where every point receives one node per unit cell. On the other hand, those for the $2 \times 2 \times 2$ superstructure have wider spread than $\mathscr{O}$ (Fig. 11, right). Importantly, the images lying close to the centre of $\mathscr{O}$ receive the full number of nodes (eight per unit cell), whereas those in the peripheral region receive less (<8). This indicates clearly that

the windows associated with the relevant six-dimensional lattice $\tilde{\mathbb{L}}_P$ should be non-uniform.

Relating the present superstructure in $\mathbb{E}$ (three-dimensional) to one in $\tilde{\mathbb{E}}$ (six-dimensional) is of significant importance in arguing further possibilities that superlattice ordering be observed in other approximants as well as quasicrystals. Indeed, it has been reported by Ishimasa (1995) that a superlattice ordering was exhibited by an icosahedral Al–Pd–Mn alloy after being annealed at 973 K. Performing a careful analysis of diffraction patterns, Ishimasa concluded that the Bravais class for the superlattice was P-type, while the corresponding six-dimensional lattice constant was $a_P = 20.881$ Å $= \tau a_F$, where τ is the golden mean and $a_F = 12.901$ Å is the *conventional six-dimensional lattice constant* for the F-type icosahedral phase Al–Pd–Mn. One can check that the equation $a_F = \tau \tilde{a}_F$ holds, where $\tilde{a}_F$ is the lattice constant of $\tilde{\mathbb{L}}_F$; hence, the conventional lattice constant is τ times that determined in the present study. The discrepancy is however non-essential since there exists an arbitrariness in choosing the basis vectors $\mathbf{a}_j$ in $\mathbb{E}$ up to the multiplication of any integral power of τ if only given the diffraction module, because of the τ-scaling invariance of the F-type icosahedral module and the corresponding I-type Fourier module (Janssen, 1986; Rokhsar *et al.*, 1987; Levitov & Rhyner, 1988). It is only because the proper scale for the cluster packing has now been fixed (§4.2) that we prefer to use $\tilde{a}_F$ instead of the conventional one a_F as the lattice constant. The lattice constant for the P-type superlattice ordering in the quasicrystal is therefore written as $a_P = \tau^2 \tilde{a}_F$. Remember that the use of the updated lattice constant would affect the order of rational approximation; *e.g.* a conventional cubic 2/1 approximant should now be called a cubic 3/2 approximant.

The simplest P-type sublattice (or superlattice) of $\tilde{\mathbb{L}}_F$ is obtained just by taking the subset whose members have only even indices, *i.e.* $\tilde{\mathbb{L}}_P^{(0)} := 2\tilde{\mathbb{L}}_P = \{[n_1 n_2 n_3 n_4 n_5 n_6]; n_j \equiv 0 \pmod 2$ for $j = 1, 2, \ldots, 6\}$. Then it is a sublattice of $\tilde{\mathbb{L}}_F$ with an index
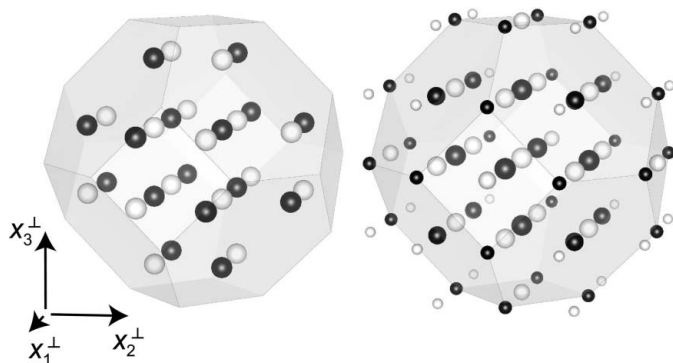
Figure 11
The modified conjugate images of the cluster centres for the ordinary 3/2 packing (left) and for the $2 \times 2 \times 2$ superstructure (right). The black (respectively, white) spheres represent the images of the centres of the B-clusters (respectively, the M-clusters). The weight (or occupancy) of each modified conjugate image is represented by the volume of the relevant sphere. The truncated octahedron $\mathscr{O}$ shown in each panel indicates the outer boundary of the fundamental domain in $\mathbb{E}_\perp$; see text for the definition.

of 32 and its six-dimensional lattice constant is given by $\tilde{a}_P^{(0)} = \tilde{a}_F$. Obviously, $\tilde{\mathbb{L}}_P^{(0)}$ fails to represent the superlattice ordering in the quasicrystal because $\tilde{a}_P^{(0)} \neq a_P (= \tau^2 \tilde{a}_F)$. In order to obtain the proper sublattice of $\tilde{\mathbb{L}}_F$ to describe the superlattice ordering of the quasicrystal, we need first to re-index $\tilde{\mathbb{L}}_F$ prior to taking the subset with only even indices. The re-indexing is done with respect to the re-scaled basis vectors $\tilde{\mathbf{a}}_j^{(2)} = (\tau^2 \mathbf{a}_j, c(-1/\tau)^2 \mathbf{a}_j^\perp)$, which can be obtained from the original basis vectors $\tilde{\mathbf{a}}_j$ through

$$(\tilde{\mathbf{a}}_1^{(2)} \tilde{\mathbf{a}}_2^{(2)} \tilde{\mathbf{a}}_3^{(2)} \tilde{\mathbf{a}}_4^{(2)} \tilde{\mathbf{a}}_5^{(2)} \tilde{\mathbf{a}}_6^{(2)})$$
$$= (\tilde{\mathbf{a}}_1 \tilde{\mathbf{a}}_2 \tilde{\mathbf{a}}_3 \tilde{\mathbf{a}}_4 \tilde{\mathbf{a}}_5 \tilde{\mathbf{a}}_6) \mathbf{M}^2, \qquad (52)$$

where six components for $\tilde{\mathbf{a}}_j$ and $\tilde{\mathbf{a}}_j^{(2)}$ are all aligned column-wise and $\mathbf{M}$ represents the uni-modular τ-scale transformation matrix (Niizeki, 1989),

$$\mathbf{M} = \frac{1}{2} \begin{pmatrix} 1 & 1 & 1 & 1 & -1 & -1 \\ 1 & 1 & 1 & -1 & 1 & -1 \\ 1 & 1 & 1 & -1 & -1 & 1 \\ 1 & -1 & -1 & 1 & -1 & -1 \\ -1 & 1 & -1 & -1 & 1 & -1 \\ -1 & -1 & 1 & -1 & -1 & 1 \end{pmatrix}. \qquad (53)$$

Note that the re-scaled basis vectors $\tilde{\mathbf{a}}_j^{(2)}$ are not orthogonal to each other if $c = 1$. Nonetheless, since the scale factor c can be arbitrarily chosen without affecting the projected images in $\mathbb{E}$, one can choose $c = \tau^4$ so that the re-scaled basis vectors are orthogonal (*cf.* $\tilde{\mathbf{a}}_j^{(2)} = \tau^2 \tilde{\mathbf{a}}_j$) and the sublattice $\tilde{\mathbb{L}}_P^{(2)}$ with even indices would regain the hyper-cubic symmetry with a six-dimensional lattice constant of $\tau^2 \tilde{a}_F$. This proves that Ishimasa's superlattice ordering is associated with the Bravais lattice $\tilde{\mathbb{L}}_P^{(2)}$. There can be another kind of P-type sublattice $\tilde{\mathbb{L}}_P^{(1)}$ defined after re-indexing with respect to the re-scaled basis vectors $\tilde{\mathbf{a}}_j^{(1)} = (\tau \mathbf{a}_j, c(-1/\tau) \mathbf{a}_j^\perp)$, which are obtained *via*

$$(\tilde{\mathbf{a}}_1^{(1)} \tilde{\mathbf{a}}_2^{(1)} \tilde{\mathbf{a}}_3^{(1)} \tilde{\mathbf{a}}_4^{(1)} \tilde{\mathbf{a}}_5^{(1)} \tilde{\mathbf{a}}_6^{(1)})$$
$$= (\tilde{\mathbf{a}}_1 \tilde{\mathbf{a}}_2 \tilde{\mathbf{a}}_3 \tilde{\mathbf{a}}_4 \tilde{\mathbf{a}}_5 \tilde{\mathbf{a}}_6) \mathbf{M}. \qquad (54)$$

When the perpendicular space $\mathbb{E}_\perp$ is scaled as $c = -\tau^2$, the six-dimensional lattice constant for $\tilde{\mathbb{L}}_P^{(1)}$ would be $\tau \tilde{a}_F$.

The three sublattices, $\tilde{\mathbb{L}}_P^{(0)}$, $\tilde{\mathbb{L}}_P^{(1)}$ and $\tilde{\mathbb{L}}_P^{(2)}$, of $\tilde{\mathbb{L}}_F$ are distinct from each other in terms of translational symmetry. One needs to clarify whether the superlattice ordering in the present approximant can be associated with the same sublattice $\tilde{\mathbb{L}}_P^{(2)}$ as in the case of the quasicrystal. In order to simplify the argument, let us focus our attention on the M-cluster whose centre lies at the body centre $\mathbf{B} = [555\overline{111}]$ of the conventional unit cell. Obviously, $\mathbf{B}$ is inequivalent to $\mathbf{V} = [000000]$, namely the vertex of the unit cell, through translation because the crystal is primitive cubic. The latter condition would be satisfied if the relevant superlattice ordering in six dimensions was described by $\tilde{\mathbb{L}}_P^{(0)}$ because the indices of $\mathbf{B}$ are all odd integers and $\mathbf{B} \notin \tilde{\mathbb{L}}_P^{(0)} (\ni \mathbf{V})$. If the superlattice $\tilde{\mathbb{L}}_P^{(1)}$ is assumed, the re-scaled indices $\mathbf{M}^{-1}[555\overline{111}] = [333\overline{111}]$ are again all odd integers, so that $\mathbf{B} \notin \tilde{\mathbb{L}}_P^{(1)} (\ni \mathbf{V})$ is again guaranteed. Yet further re-indexing of $\mathbf{B}$ leads to $\mathbf{M}^{-2}[555\overline{111}] = [222000]$, which are all even integers, and thence $\mathbf{B}$ and $\mathbf{V}$ would become equivalent through translation if the superlattice ordering was described

by $\tilde{\mathbb{L}}_P^{(2)}$. Therefore, if the superlattice ordering in the approximant had originated from the same physical mechanism as that in the quasicrystal, it would have had body-centred cubic translation symmetry. Perhaps the superlattice ordering of the approximant can be understood as a kind of lock-in phenomenon facilitated by the discreteness of the atomic surfaces, while for the quasicrystal more subtle competitions between the boundaries of atomic surfaces need to be considered (Cockayne, 1994).

5.2. Anti-phase boundaries

The atomic decorations of the eight half cubes that comprise the unit cell of the present approximant are mutually congruent in the sense that one of them can be obtained from another through a twofold rotation, a mirror reflection or the inversion. This is a strict consequence of the space group $Pa\bar{3}$; in particular, two of the half cubes that share a square face are always connected through a glide operation of the space group $Pa\bar{3}$. Although it is obvious that a half cube does not strictly fall on top of another through a half-way translation, one observes a partial overlap in the atomic positions between the two. It turns out that, from the electron diffraction pattern (Fig. 3) as well as the single-crystal X-ray diffraction data, the superlattice reflections (whose Miller indices include at least one odd number) are significantly weaker than the main reflections (whose Miller indices are all even). This indeed justifies the use of the term 'superlattice ordering' in describing the present structure though topological rearrangements are involved in doubling the translational symmetry, as opposed to a more common type of superlattice orderings associated with density or displacive modulations, for instance.

In general, the structure may not be perfectly ideal in realistic materials. For the present alloy sample, in particular, the superlattice ordering can possibly be degraded to some extent due to inequilibrium processes that may have taken place while the material was synthesized. Being inspired by the detailed description of the crystal structure (§4), we expect that the configuration of clusters within each half cube is rather strongly constrained by the local packing rules, whereas the configuration of half cubes is constrained relatively loosely. In this respect, we find that an anti-phase boundary could easily be formed by introducing only a small number of defects in the arrangement of clusters along one of the glide planes.[4] Hence, the material could have exhibited a non-negligible degradation of the superlattice ordering if it were obtained through a non-optimal cooling process. Fortunately, our sample preparation procedure (§2) yielded a high-quality approximant crystal, in which only minute structural defects are included; hence, no special care was necessary while carrying out the structure refinement.

If the sample preparation was cruder, the superlattice ordering could be violated to a significant extent. Then, the satellite Bragg reflections associated with the superlattice

ordering could be seriously damped, possibly making them undetectable. Such a circumstance may have arisen when Sugiyama and co-workers carried out a structure analysis of a closely related $Al_{70}Pd_{23}Mn_6Si$ compound which was obtained via rapid quenching (Sugiyama et al., 1998b). These authors reported that their crystal was a cubic 2/1 approximant with a lattice constant of 20.21 Å and that the space group was $Pm\bar{3}$. Note that the lattice constant is half as small as that of the present approximant. Although the reported crystal structure involving a giant icosahedral cluster (diameter >20 Å) has never indicated a reasonable connection to any other crystals in closely related alloys, the knowledge was transported to the modelling of related icosahedral quasicrystals (Yamamoto et al., 2003).

From our revised view, the halved lattice constant is likely to have resulted from failing to detect the superlattice reflections that suffered from a serious damping due to anti-phase boundaries. Hence, the previous structural solution (Sugiyama et al., 1998b) should be re-examined in view of the fact that it could correspond to the average charge-density map of the eight translates $\{\rho(\mathbf{x}+\mathbf{s})\}$ of the true charge-density map $\rho(\mathbf{x})$, where $\mathbf{s}$ runs over the eight independent translation vectors $\mathbf{0}, \mathbf{R}_1', \mathbf{R}_2', \mathbf{R}_3', \mathbf{R}_1'+\mathbf{R}_2', \mathbf{R}_2'+\mathbf{R}_3', \mathbf{R}_3'+\mathbf{R}_1'$ and $\mathbf{R}_1'+\mathbf{R}_2'+\mathbf{R}_3'$.

Let us take the superposition of the corresponding eight translates of the new crystal structure (§4.2). Here, several atomic sites can fall onto the same position with a maximal degeneracy of 8. We find that cluster-like arrangements are formed at the origin as well as at the body centre of the half-sized unit cell for the superposed structure. Fig. 12 illustrates the shell structures of the 'fake' cluster $\mathscr{I}$ at the body centre, where most of the shells exhibit the icosahedral symmetry in the geometrical arrangement except the shells $\mathscr{I}$-9 and $\mathscr{I}$-12. Note that many of these shells have a counterpart in the primary cluster reported by Sugiyama et al. (1998b). Another 'fake' cluster $\mathscr{V}$ with an icosahedral arrangement is also found at the vertex of the unit cell; see Fig. 13. Importantly, the site degeneracies of a single shell in $\mathscr{I}$ or $\mathscr{V}$ generally break the icosahedral symmetry (Figs. 12 and 13, and Table 6), where the minimal point group is $m\bar{3}$ (T_h). The violation of the icosahedral symmetry in $\mathscr{V}$ may also account for the appearance of the secondary cluster reported by Sugiyama et al. (1998b). The present argument gains further credibility as we find that the preliminary structure analysis using only the main Bragg reflections from our data set reproduces the same structure as the one reported by Sugiyama et al. (1998b) (cf. the online supplementary material).

5.3. Atomic packing

Recall that the atomic arrangement within each individual cluster is subject to constraints posed by the existence of adjacent clusters (§4.2). In turn, the atomic arrangement may hardly allow other combinations of clusters than the three cases shown in Fig. 6, thereby geometrically enforcing the even and odd subsets of the bc-packing to be differentiated. One can argue that in general the F-type ordering of a

---

[4] An anti-phase boundary is a kind of stacking fault at which the lattice planes are shifted by a half period. Structural details of anti-phase boundaries in the present material will be presented elsewhere.

Nobuhisa Fujita et al. · Al-based F-type icosahedral alloys **335**
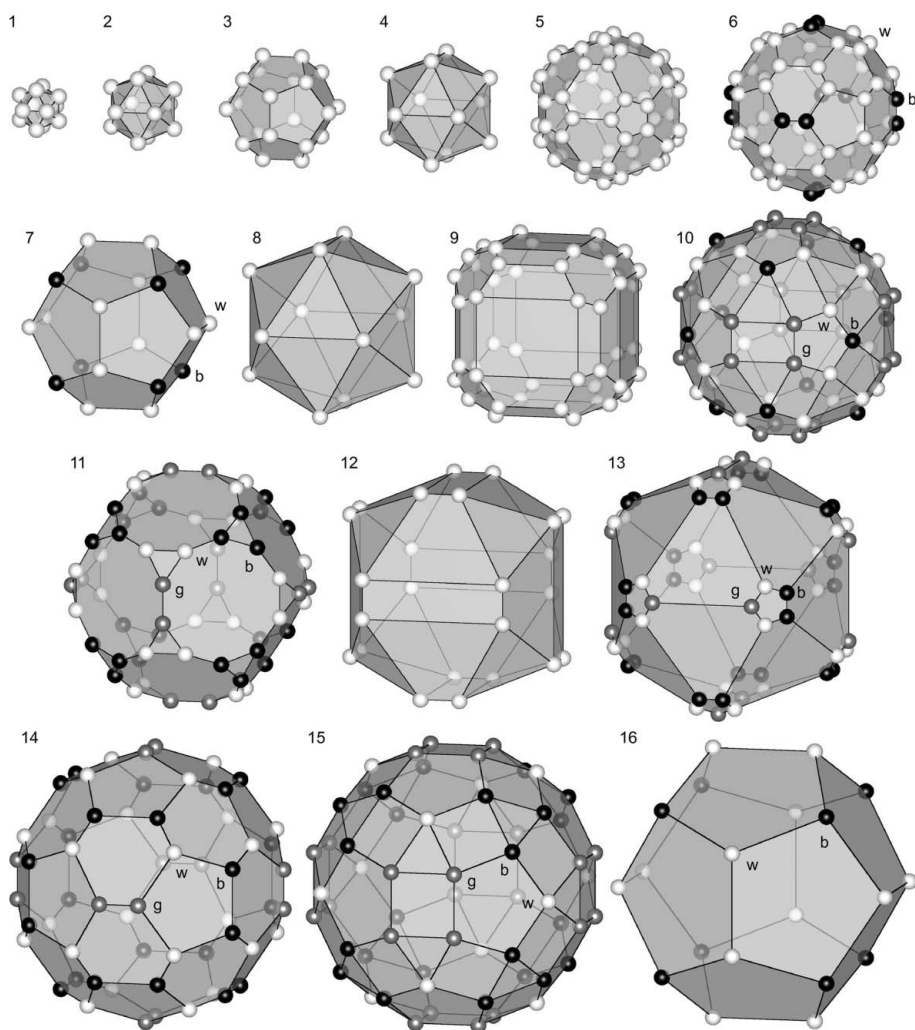
Figure 12
The 'fake' cluster $\mathscr{I}$ that is observed at the body centre of the halved unit cell in the superposition of the eight translated versions of the true structure. Each of the shells has at least the point symmetry $m\bar{3}$ (T_h) when the contents of the sites are taken into consideration. Members of a shell with different contents are distinguished by colours: white (labelled w), grey (g) and black (b).
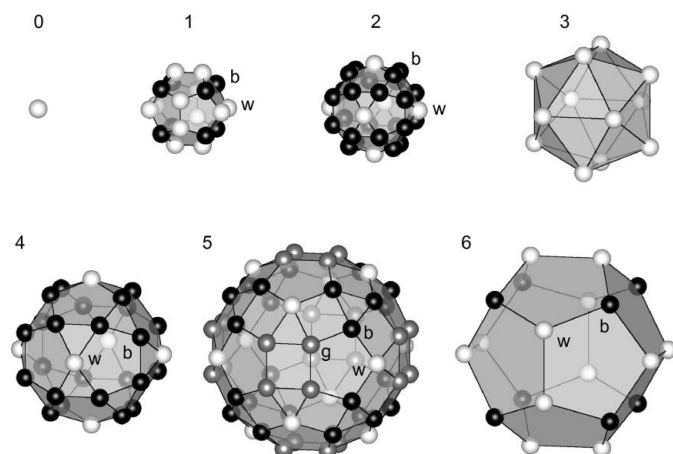
Figure 13
The 'fake' cluster $\mathscr{V}$ that is observed at the origin in the superposition of the eight translated versions of the true structure. Each of the shells has at least the point symmetry $m\bar{3}$ (T_h) when the contents of the sites are taken into consideration. Members of a shell with different contents are distinguished by colours: white (labelled w), grey (g) and black (b).

majority of stable Al-based icosahedral quasicrystals and their approximants could have a similar geometrical origin, while an uneven distribution of atomic species on the even and odd subsets of the quasi-lattice could be induced as a secondary consequence. This can be contrasted with the fact that in the literature the F-type ordering has often been associated with a simple kind of chemical ordering (Chizhikov, 2000).

As described in §4.2, the closest interatomic distances in the idealized construction include b' and c', which are parallel to two- and threefold axes, respectively. These distances are $1/\tau^2$ times smaller than b and c, respectively, so that the ratio between the two satisfies $c'/b' = c/b$ ($= 3^{1/2}/2$). In fact, this kind of local atomic ordering has been observed in a wide variety of Al-based alloys. It is given the name *dodecahedral local ordering* and has been used as a universal concept that plays a significant role in understanding various structural properties of icosahedral quasicrystals and their approximants (Dmitrienko, 1994; Dmitrienko & Chizhikov, 2006). In this respect, our cluster-based model offers a perfect realization of dodecahedral local ordering in an important class of materials with F-type icosahedral ordering.

The similarity between the packing of clusters and that of atoms might suggest that local arrangements of atoms could also be described by a tiling composed of four basic shapes, A', B', C' and D', which are the miniature versions (scale $\times 1/\tau^2$) of the canonical cells for the cluster packing. However, an essential difference exists between the two: recall that there exists an icosahedral configuration located at the centre of each B-cluster, consisting of the central site (type $\langle B_0 \rangle$) and the 12 surrounding sites (type $\langle B_5, \ldots \rangle$) forming the inner icosahedral shell. The vector from the centre to any of the 12 surrounding sites is along a fivefold axis with its length being a, which is slightly smaller than b'. Hence, an icosahedron with a dot at the centre needs to be introduced as another basic shape if a tiling description of the atomic packing is sought; we denote this shape I' (Fig. 14, left). Note that atoms will sit on both the vertices and the central dot of I'.

Another important feature peculiar to the atomic packing is the existence of two splitting sites (type $\langle M_2 \rangle$) associated with each type-I b-linkage that connects two M-clusters. Although the two sites cannot be occupied simultaneously, an Al atom is most likely jumping back and forth between these sites at a typical annealing temperature of 1123 K, where both the
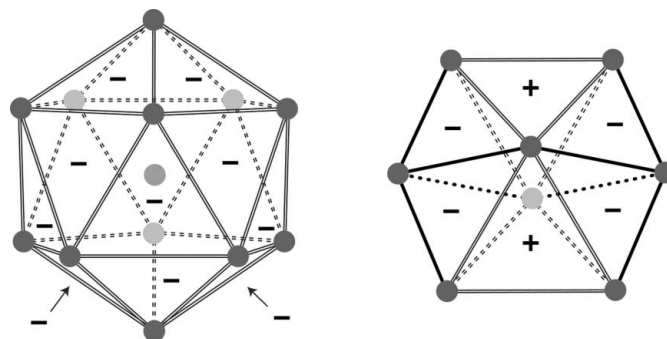
Table 6
The content of each site in the fake clusters $\mathscr{I}$ and $\mathscr{V}$, which are depicted in Figs. 12 and 13, respectively.

The shells are numbered in increasing order of radius, where the central site of $\mathscr{V}$ is numbered 0.

Shell No.	Radius (Å)	Content
Cluster $\mathscr{I}$		
1	1.738	$2\langle B_5\rangle$
2	2.813	$2\langle B_3 M_5\rangle$, $4\langle B_3^2 M_5\rangle$
3	4.144	$2\langle M_2^3\rangle$, $6\langle B_5 M_2^2\rangle$
4	4.551	$2\langle B_0\rangle$
5	5.550	$2\langle B_3 M_3\rangle$
6	6.330	w: $\langle B_5 M_2^2\rangle$, $\langle B_5 M_2\rangle$, $4\langle M_2\rangle$
		b: $2\langle B_5 M_2\rangle$, $4\langle M_2\rangle$
7	6.705	w: $6\langle B_3^2 M_5^2\rangle$, $2\langle B_3 M_5^3\rangle$
		b: $3\langle B_3^2 M_5^2\rangle$, $5\langle B_3 M_5^3\rangle$
8	7.364	$2\langle B_5 M_2\rangle$, $6\langle M_0\rangle$
9	7.935	$\langle M_2\rangle$
10	8.237	g: $\langle B_3^2 M_5\rangle$, $\langle B_3^2\rangle$, $6\langle B_3 M_3\rangle$
		w: $\langle B_3^2\rangle$, $5\langle B_3 M_3\rangle$
		b: $2\langle B_3^2 M_5\rangle$, $6\langle B_3 M_3\rangle$
11	8.782	g: $4\langle B_5 M_2^2\rangle$, $4\langle B_5 M_2\rangle$
		w: $6\langle B_5 M_2^2\rangle$, $2\langle B_5 M_2\rangle$
		b: $3\langle B_5 M_2^2\rangle$, $\langle M_2^3\rangle$, $2\langle B_5 M_2\rangle$, $2\langle M_2\rangle$
12	9.526	$2\langle B_3 M_3\rangle$
13	10.001	g: $2\langle M_2^2\rangle$, $4\langle M_2\rangle$
		w: $\langle M_2\rangle$
		b: $\langle M_2^2\rangle$, $3\langle M_2\rangle$
14	10.242	g: $4\langle B_3^2 M_5\rangle$, $4\langle B_3^2 M_5^2\rangle$
		w: $\langle B_3 M_3\rangle$, $\langle B_3^2\rangle$, $4\langle B_3^2 M_5\rangle$, $2\langle B_3^2 M_5^2\rangle$
		b: $\langle B_3 M_3\rangle$, $3\langle B_3^2 M_5\rangle$, $4\langle B_3^2 M_5^2\rangle$
15	10.685	g: $2\langle B_5 M_2\rangle$, $6\langle B_5 M_2^2\rangle$
		w: $8\langle B_5 M_2^2\rangle$
		b: $\langle M_0\rangle$, $\langle B_5 M_2\rangle$, $6\langle B_5 M_2^2\rangle$
16	10.849	w: $8\langle B_0\rangle$
		b: $5\langle B_0\rangle$
Cluster $\mathscr{V}$		
0	0.000	$8\langle M_0\rangle$
1	2.561	w: $2\langle B_3 M_3\rangle$
		b: $5\langle B_3 M_3\rangle$
2	2.957	w: $4\langle M_2\rangle$
		b: $\langle M_2\rangle$
3	4.551	$8\langle B_3^2 M_5^2\rangle$
4	4.785	w: $4\langle B_5 M_2^2\rangle$, $4\langle M_2\rangle$
		b: $7\langle B_5 M_2^2\rangle$, $\langle M_2\rangle$
5	6.604	g: $\langle B_3^2 M_5\rangle$, $5\langle B_3 M_3\rangle$
		w: $4\langle B_3^2 M_5\rangle$, $2\langle B_3 M_3\rangle$
		b: $\langle B_3^2 M_5\rangle$, $2\langle B_3 M_3\rangle$
6	6.705	w: $2\langle B_0\rangle$
		b: $5\langle B_0\rangle$

Figure 14
The two basic tiles, I' (left) and H' (right), that are necessary to provide a tiling description for the atomic positions. The double bars represent the b'-linkages, while the thick bars represent the c'-linkages between atoms. There is an atomic site for Pd at the centre of the tile I'. The surfaces of the tiles are composed of X'- and Y'-faces, which are the miniature versions of the X- and Y-faces, respectively. + or − signs shown on the front faces indicate which of the symmetrically distinguishable sides are facing outward. Note that the point symmetries of I' and H' are $\overline{5}32/m$ (I_h) and mmm (D_{2h}), respectively.
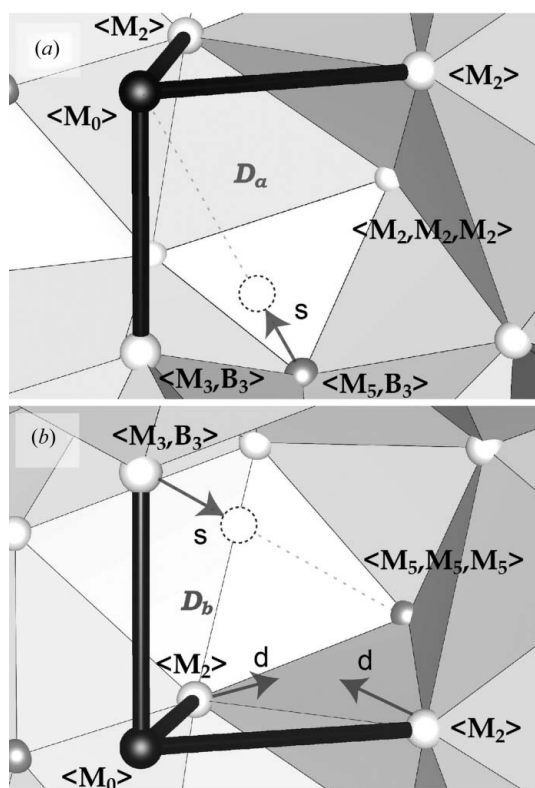
from interpenetration at its central region. This causes the inner-shell atoms of an M-cluster located at one of the vertices to be sparsely distributed towards the centre of the D-cell, thereby providing a large unfilled space or a void inside the outer shell of the M-cluster. Two relevant kinds of void are illustrated in Fig. 15 for the type-I and type-II D-cells. In the refinement of the present approximant, it is observed that a surrounding atom of such a void can have a splitting position within the void (Pd157' for Fig. 15a and Al86' for Fig. 15b) or exhibit a significant displacement towards the centre of the void (Al174' for Fig. 15b). These facts are physically consistent with the present geometrical description.

6. Concluding remarks

A simple heuristic search in the quaternary Al–Pd–Cr–Fe system has led to the first discovery of a highly stable cubic approximant phase to Al-based F-type icosahedral quasi-crystals i-Al$_{70}$Pd$_{20}$TM$_{10}$ (TM = transition metals). Single crystals of the approximant a few hundred μm in diameter have been grown with slow cooling, suggesting that the approximant phase is formed congruently from the melt. Using single-crystal X-ray diffraction, an *ab initio* structure analysis has been carried out successfully, revealing a crystal symmetry of $Pa\overline{3}$ with a lattice constant of 40.5 Å. All the atoms in the crystal belong to two kinds of clusters which are referred to as the pseudo-Mackay-type and the mini-Bergman-type clusters, whereas there is no need for glue atoms.

The centres of the clusters are located at the vertices of a CCT, designated as a $2 \times 2 \times 2$ superstructure of the 3/2 packing (Henley, 1991), in which the parity of each vertex determines unambiguously the kind of the relevant cluster. Importantly, the present structure offers a set of universal rules for the local packing of clusters. The rules are applicable

splitting sites play an inevitable role in maintaining and stabilizing the structure. The two splitting sites are always located at the two tips of a flat hexagonal bipyramid, which corresponds to the overlap of two adjacent M-clusters. We denote this shape H' (Fig. 14, right). The two tips of H' are the very splitting sites of the type $\langle M_2\rangle$, while the six vertices of the base hexagon include two atomic sites that are symbolized as $\langle M_5, M_5, \ldots\rangle$ and four that are symbolized as $\langle M_2, M_2, \ldots\rangle$.

The idealized atomic arrangement can now be represented as an arrangement of the six basic geometrical shapes A', B', C', D', I' and H'. Still, it may not be called a tiling because a part of the space is left blank in this description. The latter circumstance arises when the cluster packing involves any number of D-cells. Remember that a D-cell has the largest volume among the four canonical cells and clusters are free

Figure 15
Two kinds of voids associated with D-cells. (a) A void within the outer shell of an M-cluster located at a corner D_a of a type-I D-cell. The edges of the D-cell are represented as black bars. The spheres are the atomic positions predicted by the present geometrical rules, where labels for some atomic sites are presented in the figure. (b) Similar to (a) but the void is associated with a corner D_b of a type-II D-cell. A splitting position for an atomic site is indicated with an arrow and a dotted circle (labelled 's'). A possible atomic displacement is indicated with an arrow (labelled 'd'). In the refinement, the two kinds of splitting positions as in (a) and (b) are included as Pd157' and Al86', respectively.

to arbitrary CCTs, whereby a number of hypothetical approximants can be constructed. Some of these hypothetical structures could be synthesized in related alloys. Indeed, the crystal structure that was previously reported as a cubic 1/1 approximant by Sugiyama *et al.* (1998a) could be better understood as an artifact of folding a hypothetical structure constructed from a 2 × 2 × 2 superstructure of the 2/1 packing (Henley, 1991) into a half-sized unit cell. Here a similar argument to that presented in §5.2 is assumed. A search for stable approximants with various degrees of rational approximation to τ within related alloy systems is an important future challenge.

In actual fact, the proposed two cluster units, M and B, have been already used (with a somewhat different way of handling the inner shell of the M-cluster) to compose a hypothetical model of F-type icosahedral quasicrystals, *e.g.* i-Al–Pd–Mn (Elser, 1996; Gratias *et al.*, 2000). In this case, the clusters are assumed to be centred at the vertices of a random rhombohedral tiling composed of the two kinds of Ammann rhombohedra. Here, individual clusters are connected with their adjacent neighbours through the edges (in fivefold directions)

or the short diagonals (in twofold directions) of the rhombic faces, whereas clusters at the two ends of the short body diagonal (along a threefold direction) of each obtuse rhombohedron are forced to be interpenetrated heavily with each other. Our findings proved to be against this model, since no pair of clusters connected through a fivefold or a short threefold linkage is observed in the reconstructed crystal structure.

The superlattice ordering in the icosahedral quasicrystal, i-Al–Pd–Mn (Ishimasa & Mori, 1992) has attracted much attention, and rich features associated with this phenomenon have been published (de Boissieu *et al.*, 1998; Audier *et al.*, 1999; Letoublon *et al.*, 2000; Hirai *et al.*, 2000). However, no clear account of its physical origin has been provided, although it seems to be closely related to the binary cluster composition for the F-type icosahedral systems. In the expectation that the superlattice ordering in the present approximant may be related to that in the quasicrystal, possible P-type superlattice orderings in the six-dimensional F-type hyper-cubic lattice have been analysed in §5.1, where it has turned out that the two phenomena cannot be associated with the same six-dimensional superlattice. A kind of a lock-in transition into the 2 × 2 × 2 superstructure might have occurred in the approximant in favour of a slight increase of the packing density of clusters, whereas in the quasicrystal more subtle competitions between the boundaries of atomic surfaces could be responsible for it.

One of the most important outcomes of this work is the finding that the atomic arrangement is perfectly described using a set of geometrical rules for cluster packing defined on a CCT. Local arrangements of atomic positions thus determined can be described generally as the vertices of six basic polyhedra A′, B′, C′, D′, I′ and H′, which are arranged under the face-to-face matching constraint. Importantly, the latter construction leaves the presence of a void inside the outer shell of each M-cluster that is located at a vertex of a D-cell. The present structure refinement has indicated that some of the surrounding atoms of the voids have a splitting position within the void or exhibit a significant displacement towards the centre of the void.

Altogether, the present results have greatly improved our understanding of the local atomic structures of F-type icosahedral quasicrystals and their approximants. Clearly, the present local rules for cluster packing maintain a certain level of universality, and a variety of complex structures that are closely related to Al-based F-type icosahedral quasicrystals are expected to be described within the same framework. However, when the structure of the quasicrystal is at stake, there remains a crucial issue of whether the canonical cells can be used to construct a quasiperiodic tiling with the icosahedral symmetry. The peculiar shapes of the canonical cells are known to impose non-local geometrical constraints, making it difficult to determine their non-periodic alignments throughout the whole space. It is an important challenge in the theoretical crystallography of quasicrystals to prove if an icosahedral quasiperiodic tiling can be constructed using the canonical cells.

APPENDIX *A*
Derivation of the statistics formulae for the 16 types of atomic sites

Note that each class of atomic site is associated with one or more type(s) of geometric objects (see Fig. 8 and Table 5), and a careful inspection of the decorated objects proves the following relationships:

$$n(\text{node}_\text{I}) = f = (h + m)/20 = (n + 3r + s + 2t + 3u)/12$$
$$= (g + 2k + l + 2p + 3q)/30, \tag{55}$$

$$n(\text{node}_\text{II}) = i = (j + l + p)/12$$
$$= (m + n + 2o + 2s + 2t + u)/20, \tag{56}$$

$$n(b_\text{I}) = g/2 = (3r + t + 3u)/2 = (k + p + 3q)/4, \tag{57}$$

$$n(b_\text{II}) = (o + s + t)/2, \tag{58}$$

$$n(c) = m = (l + 2p)/3 = (n + 2s + 4t + 3u)/3, \tag{59}$$

$$n(\text{X}_\text{I}) = p = 2t + 3u, \tag{60}$$

$$n(\text{X}_\text{II}) = s + 2t, \tag{61}$$

$$n(\text{Y}_\text{I}) = q = r + u, \tag{62}$$

$$n(\text{A}_\text{I}) = t, \tag{63}$$

$$n(\text{C}_\text{I}) = u, \tag{64}$$

where the variables $f, g, \ldots, u$ represent the number frequencies for the 16 types of atomic sites. Some of these equations turn out to be redundant in the sense they are not necessarily independent of each other. By solving these equations, equations (32)–(47) of §4.3 can be readily obtained.

APPENDIX *B*
Refined parameters

Among the 4728 atomic positions contained in a single unit cell, 4680 are reproduced (within small deviations) by replicating the cluster templates at the vertices of the CCT under the geometrical rules fully described in §4.2. The remaining 48 positions are irregular splitting sites (Al86′ and Pd157′) introduced inside voids associated with M-clusters centred at Fe/Pd82 and Cr/Al98. The inclusion of these splitting sites has reduced $R_\text{w}(F)$ by more than 1%. Bear in mind that no glue atom is included in the structure.

The existence of voids causes some additional irregularities for the refinement. (i) The splitting site Pd157′ appears to contradict with the site Al/Cr104 which lies nearby. Therefore, the total s.o.f. (site-occupation factor) of Al/Cr104 is set to be equal to that of Pd157, so that it complements that of Pd157′. (ii) In addition, the atomic site Al174′ shifted towards the centre of a void lies too close to Al183, whereas the distance between Al174 and Al174′, which are originally splitting sites for a single Al atom, is large enough to accommodate atoms at both of them. Therefore, s.o.f.'s for the four positions Al174,

Al174′, Al183, Al183′ are refined so that their sum is fixed to 2. These are exceptional measures that we have taken to achieve reasonable convergence of the refinement.

The number of independent atomic positions cannot be reduced below 204. In an effort to suppress the number of independent parameters, the following three constraints on the isotropic atomic displacement parameters (IADPs) are introduced. (i) Within the inner shell of each B-cluster, the IADPs are set to be identical for the same site class. See, for example, the IADPs of Al12, ..., Al23 in Table 7;[5] the IADPs for the site classes $\langle B_5, M_2, M_2 \rangle$, $\langle B_5, M_2 \rangle$ and $\langle B_5 \rangle$ are 0.015, 0.01 and 0.006, respectively. (ii) The IADPs for the two splitting sites associated with each *b*-linkage between M-clusters are set to be identical; *e.g.* the IADPs for Al173 and Al173′ are both 0.029. (iii) In the final stage of the refinement, it was found that the IADP and the s.o.f. are strongly correlated for Fe/Pd154. If both the parameters are refined, the IADP converges to a negative value while the Pd concentration reduces by more than 10%. Hence, the IADP of this atomic site is fixed to be 0.011.

In Table 7, it is observed that IADPs for some atomic positions in the inner shell of M-clusters are exceptionally large (*e.g.* Al96, Al97, Al00 and Al/Cr104). This might be due to possible disorders in the M_3 shells. A full characterization of such disorders may require a detailed analysis of charge-density distributions for the M_3 shells. However, the quality of our intensity data may not be sufficient for performing such an analysis.

References

Audier, M., Duneau, M., de Boissieu, M., Boudard, M. & Letoublon, A. (1999). *Philos. Mag. A*, **79**, 255–270.
Boissieu, M. de, Boudard, M., Ishimasa, T., Elkaim, E., Lauriat, J. P., Letoublon, A., Audier, M., Duneau, M. & Davroski, A. (1998). *Philos. Mag. A*, **78**, 305–326.
Bruker (2001). *SMART* (Version 5.625), *SAINT* (Version 6.45) and *SADABS*. Bruker AXS Inc., Madison, Wisconsin, USA.
Chizhikov, V. A. (2000). *Crystallogr. Rep.* **45**, 122–127.
Cockayne, E. (1994). *Phys. Rev. B*, **49**, 5896–5910.
Dmitrienko, V. E. (1994). *Acta Cryst.* A**50**, 515–526.
Dmitrienko, V. E. & Chizhikov, V. A. (2006). *Crystallogr. Rep.* **51**, 552–558.
Dmitrienko, V. E. & Chizhikov, V. A. (2007). *Crystallogr. Rep.* **52**, 1040–1047.

---

[5] Table 7 is available from the IUCr electronic archives (Reference: DM5040). Services for accessing this table are described at the back of the journal.

Duneau, M. & Oguey, C. (1989). *J. Phys. Fr.* **50**, 135–146.

Elser, V. (1985). *Phys. Rev. B*, **32**, 4892–4898.

Elser, V. (1996). *Philos. Mag. B*, **73**, 641–656.

Elser, V. & Henley, C. L. (1985). *Phys. Rev. Lett.* **55**, 2883–2886.

Gratias, D., Quiquandon, M. & Katz, A. (2000). *Quasicrystals: Current Topics*, edited by E. Belin-Ferre, C. Berger, M. Quiquandon & A. Sadoc, pp. 1–72. Singapore: World Scientific.

Henley, C. L. (1986). *Phys. Rev. B*, **34**, 797–816.

Henley, C. L. (1991). *Phys. Rev. B*, **43**, 993–1020.

Hirai, I., Ishimasa, T., Letoublon, A., Boudard, M. & de Boissieu, M. (2000). *Mater. Sci. Eng. A*, **294–296**, 33–36.

Ishimasa, T. (1995). *Philos. Mag. Lett.* **71**, 65–73.

Ishimasa, T. & Mori, M. (1992). *Philos. Mag. B*, **66**, 513–532.

Janssen, T. (1986). *Acta Cryst.* A**42**, 261–271.

Letoublon, A., Ishimasa, T., de Boissieu, M., Boudard, M., Hennion, B. & Mori, M. (2000). *Philos. Mag. Lett.* **80**, 205–213.

Levitov, L. S. & Rhyner, J. (1988). *J. Phys.* **49**, 1835–1849.

Mihalkovic, M. & Mrafko, P. (1993). *Europhys. Lett.* **21**, 463–467.

Mihalkovic, M., Zhu, W.-J., Henley, C. L. & Oxborrow, M. (1996). *Phys. Rev. B*, **53**, 9002–9020.

Momma, K. & Izumi, F. (2008). *J. Appl. Cryst.* **41**, 653–658.

Newman, M. E. J., Henley, C. L. & Oxborrow, M. (1995). *Philos. Mag. B*, **71**, 991–1013.

Niizeki, K. (1989). *J. Phys. A: Math. Gen.* **22**, 4295–4302.

Palatinus, L. & Chapuis, G. (2007). *J. Appl. Cryst.* **40**, 786–790.

Petricek, V., Dusek, M. & Palatinus, L. (2006). *JANA2006. The Crystallographic Computing System*. http://jana.fzu.cz/. Institute of Physics, Prague, Czech Republic.

Rokhsar, D. S., Mermin, N. D. & Wright, D. C. (1987). *Phys. Rev. B*, **35**, 5487–5495.

Sugiyama, K., Kaji, N., Hiraga, K. & Ishimasa, T. (1998a). *Z. Kristallogr.* **213**, 168–173.

Sugiyama, K., Kaji, N., Hiraga, K. & Ishimasa, T. (1998b). *Z. Kristallogr.* **213**, 90–95.

Takakura, H., Gomez, C. P., Yamamoto, A., de Boissieu, M. & Tsai, A. P. (2007). *Nat. Mater.* **6**, 58–63.

Tsai, A. P., Inoue, A., Yokoyama, Y. & Masumoto, T. (1990). *Mater. Trans. JIM*, **31**, 98–103.

Yamamoto, A., Takakura, H. & Tsai, A. P. (2003). *Phys. Rev. B*, **68**, 094201.